Quantification of macrophage-driven inflammation during myocardial infarction with 18F-LW223, a novel TSPO radiotracer with binding independent of the rs6971 human polymorphism

Journal of Nuclear Medicine, published on August 28, 2020 as doi:10.2967/jnumed.120.243600

Quantification of macrophage-driven inflammation during myocardial infarction with ^{18}F-LW223, a novel TSPO radiotracer with binding independent of the rs6971 human polymorphism

Authors

Mark G. MacAskill[1,2], Agne Stadulyte[1,2], Lewis Williams[3], Timaeus E. F. Morgan[3], Nikki L. Sloan[3], Carlos J. Alcaide-Corral[1,2], Tashfeen Walton[1,2], Catriona Wimberley[2,4], Chris-Anne McKenzie[5], Nick Spath[1], William Mungall[6], Ralph BouHaidar[7], Marc R. Dweck[1], Gillian A. Gray[1], David E. Newby[1], Christophe Lucatelli[2], Andrew Sutherland[3], Sally L. Pimlott[8,9], Adriana A.S. Tavares[1,2*.]

Affiliations

[1]University/BHF Centre for Cardiovascular Science, University of Edinburgh, Edinburgh, UK.

[2]Edinburgh Imaging, University of Edinburgh, Edinburgh, UK.

[3]WestCHEM, School of Chemistry, University of Glasgow, UK.

[4]Centre for Clinical Brain Sciences, University of Edinburgh, Edinburgh, UK.

[5]MRC Edinburgh Brain Tissue Bank, University of Edinburgh, UK.

[6]Bioresearch and Veterinary Services, University of Edinburgh, UK.

[7]Forensic Pathology, University of Edinburgh, UK.

[8]School of Medicine, University of Glasgow, UK.

[9]NHS Greater Glasgow and Clyde, UK.

*Corresponding Author

Key Words

TSPO, PET, Macrophage, Inflammation, Myocardial Infarction

First Author Contact Information

CVS, The Queen's Medical Research Institute,

Edinburgh BioQuarter,

47 Little France Crescent

Edinburgh

EH16 4TJ

Tel: 0131 242 6735

Email: Mark.MacAskill@ed.ac.uk

Corresponding Author Contact Information

CVS, The Queen's Medical Research Institute,

Edinburgh BioQuarter,

47 Little France Crescent

Edinburgh

EH16 4TJ

Tel: 0131 242 7975

Email: Adriana.Tavares@ed.ac.uk

ABSTRACT

Rationale: Myocardial infarction (MI) is one of the leading causes of death worldwide and inflammation is central to the tissue response and patient outcomes. The 18kDa translocator protein (TSPO) has been utilized in positron emission tomography (PET) as an inflammatory biomarker. The aims of this study were to: 1) screen novel, fluorinated, TSPO radiotracers for susceptibility to the rs6971 genetic polymorphism using *in vitro* competition binding assays in human brain and heart, 2) assess whether the *in vivo* characteristics of our lead radiotracer, ^{18}F-LW223, are suitable for clinical translation and 3) validate whether ^{18}F-LW223 can detect macrophage driven inflammation in a rat myocardial infarction model.

Methods: Fifty-one human brain and twenty-nine human heart tissue samples were screened for the rs6971 polymorphism. Competition binding assays were conducted with ^{3}H-PK11195 and the following ligands: PK11195, PBR28 and our novel compounds (AB5186 and LW223). Naive rats and mice were used for *in vivo* PET kinetic studies, radiometabolite studies and dosimetry experiments. Rats underwent permanent coronary artery ligation and were scanned using PET/CT with invasive input function at 7 days following MI. For quantification of PET signal in the hypoperfused myocardium, K_1 was used as a surrogate marker of perfusion to correct the binding potential for impaired radiotracer transfer from plasma to tissue (BP_{TC}).

Results: LW223 binding to TSPO was not susceptible to the rs6971 genetic polymorphism in human brain and heart samples. In rodents, ^{18}F-LW223 displayed a specific uptake consistent with TSPO expression, a slow metabolism in blood (62% of parent at 120 min), a high plasma free fraction of 38.5% and a suitable dosimetry profile

(effective dose of 20.5-24.5 μSv/MBq). ^{18}F-LW223 BP_{TC} was significantly higher in the MI cohort within the infarct territory of the anterior wall relative to the anterior wall of naive animals (36.9±8.8 vs. 10.0±2.4 cm^3/mL/min, p≤0.001). *Ex-vivo* immunofluorescent staining for TSPO and CD68 (macrophage marker) resulted in the same pattern seen with *in vivo* BP_{TC} analysis.

Conclusion: ^{18}F-LW223 is not susceptible to the rs6971 genetic polymorphism in *in vitro* assays, has favorable *in vivo* characteristics and is able to accurately map macrophage driven inflammation following MI.

INTRODUCTION

Cardiovascular disease is the leading cause of morbidity and mortality worldwide (*1*). A large proportion of these fatalities is due to myocardial infarction (MI). Acute inflammation is a key driver of pathology determining disease perturbation following tissue infarction (*2*). Therefore, an urgent need exists for a non-invasive imaging technology to act as a prognostic tool and predict subsequent patient outcomes.

The 18kDa translocator protein (TSPO) is expressed within the outer membrane of the mitochondria (*3*) where it is a key factor in controlling the transport of cholesterol necessary for steroid hormone synthesis. TSPO is highly expressed within inflammatory cells such as macrophages in the periphery (*4*) and microglia in the brain (*5*), and has consequently been used as a marker of inflammation in pathologies throughout the body (*4*,*6*–*10*).

Despite TSPO being one of the most widely explored targets in the field of Positron Emission Tomography (PET), clinical adoption of this tissue biomarker has been globally hindered by radiotracers with suboptimal properties. For example, the prototypical TSPO ligand ^{11}C-PK11195 (*11*) has relatively high non-specific binding and a short half-life (*12*). Efforts to surpass the limitations of ^{11}C-PK11195 have been hampered primarily by the differential binding of second generation TSPO radiotracers now known to be caused by the rs6971 genetic polymorphism (*13*). Moreover, the use of TSPO PET radiotracers in the context of cardiovascular disease, in particular following MI, has faced limited adoption due to lack of validated paradigms for quantification of regional tissue inflammation in hypoperfused areas using a single technique/single scan. Previously, quantification of regional tissue inflammation following MI has relied on the use of TSPO

PET static imaging and Single Photon Emission Computed Tomography (SPECT) perfusion static scans for correction of the TSPO PET data (*6*). Consequently, there is a need to develop improved TSPO PET ligands and methodology to boost adoption of this technology for non-invasive imaging of inflammation in cardiology.

This study aims to: 1) screen novel, fluorinated, TSPO radiotracers for susceptibility to the rs6971 genetic polymorphism using the gold standard *in vitro* competition binding assays in human brain and heart, 2) assess whether the *in vivo* characteristics of our lead radiotracer is suitable for clinical translation and 3) validate whether our novel TSPO radiotracer can detect macrophage driven inflammation in a rat myocardial infarction model.

MATERIALS AND METHODS

Radiotracer Preparation

A four-step synthetic strategy was developed for the preparation of the chloride precursor and LW223 (Supplemental Fig.1). Initially, the starting material 3-methyl-4-phenylquinoline-2-carboxylic acid was prepared as previously reported by us (*14*). This was converted to the (*R*)-*sec*-butylamide by coupling with (*R*)-*sec*-butylamine and using the coupling agent HBTU. Under standard basic conditions, the amide was subjected to an *N*-methylation. The key step then involved a radical-mediated bromination of the 3-methyl substituent using *N*-bromosuccinimide and the radical initiator benzoyl peroxide. The resulting bromide intermediate was then converted to the chloride or LW223 using lithium chloride or sodium fluoride, respectively. All intermediates and final compounds were purified by column chromatography and characterized using a combination of NMR

spectroscopy and mass spectrometry (see organic chemistry section within the supplemental file for details (*14*,*15*)). The two amide rotamers of LW223 were separated and characterized by LC-MS (Supplemental Fig.2).

^{18}F-LW223 was prepared as shown in Figure.1, using the GE TRACERlab® FX_{FN} synthesizer. The radiotracer was purified by semi-preparative High Performance Liquid Chromatography using the following conditions: C18 Synergi Hydro-RP 80 Å, 150×10 mm, 4 µm column (Phenomenex, UK), acetonitrile/water (70:30 v/v) and flow rate of 3 mL/min. ^{18}F-LW223 was formulated in 10% ethanol in saline. The average radioactivity yield was 50±4% (starting from 22±3 GBq of ^{18}F-fluoride, *n* = 34) after a total synthesis time of 55 minutes. The identity of ^{18}F-LW223, radiochemical purity (>99%) and molar activity (89±12 GBq/µmol, *n* = 34) were determined by High Performance Liquid Chromatography analysis at the end of synthesis.

In Vitro Competition and Saturation Binding Assays with Human Tissue

All studies using human tissue were conducted in accordance with the National Health Service Research Ethics Committee South East Scotland (NHS-RECSE, Edinburgh Brain and Tissue Bank, 16/ES/0084). Supplemental Table.1 contains the BNN reference number for all tissues utilized from the Edinburgh Brain and Tissue Bank. Fifty-one brain (78% male, age 53.9±9.5) and twenty-nine heart (83% male, age 48.2±13.2) samples were obtained and screened for the rs6971 genetic polymorphism and grouped into HAB, MAB or LAB as previously described (*13*). Samples were homogenized in 10× w/v buffer (50 mM Tris-Base, pH 7.4, 4 ºC) before centrifugation (32,000 g, 10 min, 4 ºC). Tissue pellets were then resuspended in 10× w/v buffer and centrifuged again before

resuspending in 2 mL of buffer. Samples were assessed for protein concentration using the Bio-Rad protein assay (Bio-Rad, USA), aliquoted and stored at -80 ºC until use. The competition binding assay protocol was adjusted from a previously reported protocol (*16*), as detailed within the supplementary file.

Animals and Surgical Procedures

All experiments were authorized by the local University of Edinburgh animal welfare and ethical review committee and in accordance with the Home Office Animals (Scientific Procedures) Act 1986. Thirty-three adult male Sprague-Dawley rats (312.1± 15.0 g), and thirteen C57Bl/6 (8 male, 5 female, 25.5± 1.5 g) were used for this study. The animals were housed under standard 12 h light:12 h dark conditions with food and water available *ad libitum*. On the day of the experiment, anesthesia was induced and maintained with 1.5–2.5% isoflurane (50/50 oxygen/nitrous oxide, 1 l/min). For imaging experiments, an intravenous (i.v.) line was established in the femoral vein or tail vein for injection of the radiotracer and the femoral artery was cannulated to allow automated blood sample collection, as previously described (*17*). In a separate set of experiments (radiometabolite studies), the femoral artery was cannulated for blood sampling and the radiotracer was administered i.v. via tail vein. Surgical cannulation of femoral vein and artery was performed as detailed in the supplementary file.

Body temperature was maintained by heated scanner bed or heated mat and monitored by rectal thermometer. Vital signs, including heart rate and respiration rate were monitored continuously during the experiments.

For MI studies, anesthesia was induced and maintained using isoflurane (0.5-3% in 1.0 l/min oxygen) before buprenorphine (0.05 mg/kg, Alstoe Ltd, York, UK) was administered preoperatively for analgesia. Tracheal intubation was achieved under direct vision, and ventilation was maintained with a rodent ventilator (Harvard Apparatus Model 683, MA, USA, tidal volume 2.5 cm^3, respiratory rate 60/min). Myocardial infarction was induced as we have previously described (*18*) and further details can be found in the supplementary file. Animals were imaged on day 7±1 post-MI, referred to as day 7 throughout the manuscript.

In Vivo **PET Imaging**

Study Design

Thirty-two PET scans were performed with ^{18}F-LW223 (17.8± 1.5 MBq, bolus i.v., mean± standard error of the mean (SEM)). Naive and MI rat scans were acquired immediately following i.v. bolus injection of ^{18}F-LW223. Blocking studies were carried out in rats with PK11195 (1 mg/kg, i.v.) 30 min prior to receiving ^{18}F-LW223. For displacement studies, rats received ^{18}F-LW223 and were scanned continuously for 120 min, with single dose of PK11195 (1 mg/kg, i.v.) administered at the 60 min time-point. Dosimetry studies were conducted using mice and 240 min PET scans.

Arterial Input Functions

A commercially available system (Twilite2, Swisstrace, Switzerland) was used for the measurement of blood radioactivity as previously described (*17*). The whole-blood

arterial input function measured by the automatic blood sampler was corrected for the plasma-to-whole blood ratio and for metabolism *in vivo*.

Image Acquisition and Reconstruction

Data were acquired using a PET/CT small animal scanner (nanoPET/CT, Mediso, Hungary). A CT scan (semi-circular full trajectory, maximum field of view, 480 projections, 50 kVp, 300 ms and 1:4 binning) was acquired for attenuation correction. Immediately following radiotracer administration, a 120 or 240 minutes emission scan was obtained using 3-dimentional 1:5 mode and re-binned as follows: Rat studies= 18×10 sec; 2×30 sec; 1×60 sec; 2×2 min; 10×5 min; 6×10 min or 18×10 min, Mouse studies=4×5 min, 4×10 min, 9×20 min. Rat PET studies were reconstructed using Mediso's iterative Tera-Tomo 3D reconstruction algorithm, which includes point spread correction, and the following settings: 4 iterations, 6 subsets, full detector model, low regularization, spike filter on, voxel size 0.4 mm and 400-600 keV energy window. Mouse dosimetry PET data were reconstructed using filtered back projection (FBP) and the following settings: voxel size 0.4 mm and 400-600 keV energy window. All PET data were corrected for randoms, scatter and attenuation.

Image Processing and Data Analysis

Reconstructed scans were imported into PMOD version 3.8 (PMOD Technologies, Switzerland). Volumes of interest (VOIs) were manually drawn around the brain, heart and lung using CT images. To sample the infarct area (or equivalent area in naïve hearts) averaged PET images (0-120 minutes) were used to place three spherical VOIs at the

centre of the infarct territory within the ventricular wall (1.5 mm^3). Only the right lung was used for analysis in MI rats to avoid surgical induced trauma (left lung is deflated during the surgical procedure). Time-activity curves were generated and standard uptake values (SUVs) calculated as concentration in the VOI divided by injected dose divided by animal weight. Kinetic modelling was performed using the two-tissue compartment model to estimate the kinetic rate constants K_1 to k_4 and V_T in different tissues. V_B was not modelled in this study. Two-tissue modelling was selected as the preferred model based on a comparison of goodness and robustness of fitting versus several other models (Supplemental Fig.3 and Supplemental Table.2). The binding potential relative to non-displaceable volume (BP_{ND}) was defined as k_3/k_4 (*19*). The transfer corrected BP_{ND}, termed BP_{TC}, was formulated as below:

$$BP_{TC} = \frac{k_3}{k_4} \div K_1 \qquad \text{Eq. 1}$$

where k_3=radiotracer association rate with specific binding, k_4=dissociation rate constant of target-ligand and K_1=rate constant for transfer from arterial plasma to tissues. When tissue blood flow is impaired, such as post-MI, K_1→blood flow, as per Renkin-Crone equation:

$$K_1 = F \times E = F\,(1 - e^{-\frac{PS}{F}}) \qquad \text{Eq. 2}$$

where F=flow, E=extraction and PS=permeability.

Dosimetry

Reconstructed whole-body PET scans were imported into PMOD 3.8 and VOIs were drawn around organs that displayed higher radioactivity concentration than background, i.e. source organs. The following organs were identified as source organs;

brain, heart, lung, gallbladder, liver, gut, adrenals, kidneys and bladder. A whole-body VOI was drawn around the animal body and was used for quantification of whole-body remainder activity as whole-body activity minus source organs activity. At each time point, the measured activity of the source organs were expressed as the percent injected dose (%ID). The residence time τ, defined as the ratio of accumulated activity in the target organ ($\bar{A}$) and injected activity (A_0); $\tau=\bar{A}/A_0$(*20*), was calculated as previously described (*21*). Calculated τ were normalized based on the factors shown in Supplemental Table.3 (*22*–*26*) and entered into OLINDA/EXM 1.0 software to estimate organ doses and effective doses.

Radiometabolite Blood and Tissue Processing and Analysis

Arterial blood samples were collected at 2, 5, 10, 20, 30, 60 and 120 minutes; heart, lung and brain tissue samples were collected at 60 and 120 minutes post-radiotracer injection (69.7±9.1 MBq, mean±SEM, *n* =17 rats). Blood and tissues were processed as detailed in the supplementary file.

***Ex Vivo* Immunofluorescence Imaging**

Naive and MI heart tissue was fixed in 10% neutral buffered formalin for 24 hours, wax processed and sectioned. The CD68 (a macrophage marker) and TSPO stain was carried out using a double tyramide signal amplification (TSA) visualization as described previously (*27*). Mouse and rabbit IgG at an equal concentration served as an isotype control. Full details on immunohistochemistry tissue processing protocols used can be found in the supplementary file.

Whole tissues were imaged using an Axio Scan.Z1 slide scanner (Zeiss, Germany). Quantification was performed using Image J (v1.49, NIH, USA) by selecting regions of interest and quantifying the mean intensity for each channel of interest.

General Statistical Analysis

GraphPad Prism version 6 (GraphPad Software Inc., USA) was used for data fitting, statistical analysis and production of graphs. In competition binding assays and saturation assays, outliers within experimental triplicates were removed using a Grubbs test with an alpha of 0.2. Two-way ANOVA with post-hoc Sidak, Pearson correlations and unpaired and paired *t*-tests were used in this study for comparison between two groups, as indicated within the relevant figure legends, with a $p<0.05$ considered statistically significant. All error bars represent the standard error of the mean (SEM), unless otherwise indicated in the figure or table legends.

RESULTS

Binding of Our Lead Compound, LW223, To TSPO Is Not Affected By the rs6971 Polymorphism in *In Vitro* Assays

The inhibition constant (*Ki*) (*28*) of PK11195, two PK11195 analogues (AB5186 (*29*) and LW223, our lead compound) and PBR28 (Fig.2.A) were investigated in this study. Saturation assays were used to determine the K_d of PK11195 (Supplemental Fig.4).

In the human brain, PK11195 *Ki* was unaffected by the genetic polymorphism (Fig.2.B, Left), unlike PBR28 (Fig.2.B, Middle Left). AB5186 *Ki* was affected by the

genetic polymorphism (Fig.2.B, Middle Right), unlike LW223, which was unaffected (Fig.2.B, Right). There were no differences between HAB and LAB in PK11195 and LW223 binding studies (Supplemental Fig.5.A and G). Conversely, *Ki* values in HAB and LAB for PBR28 and AB5186 revealed differences between groups (Supplemental Fig.5.C and E). LW223 mean *Ki* was 0.6 nM, twice higher than PK11195.

In the human heart, the *Ki* of PK11195 was independent of the genetic polymorphism (Fig.2.C, Left). PBR28 and AB5186 were also affected to a similar degree in the heart as in the brain (Fig.2.C, Middle Left and Middle Right). LW223 binding in the heart was unaffected by the polymorphism (Fig.2.C, Right). *Ki* values for all heart samples demonstrated no differences between HAB and LAB in PK11195 and LW223 binding studies (Supplemental Fig.5.B and H). In the heart, LW223 mean *Ki* was the same as PK11195 at 1.7 nM. Individually calculated *Ki* values for PBR28 and AB5186 revealed a difference between HAB and LAB (Supplemental Fig.5.D and F).

^{18}F-LW223 Binds to TSPO *In Vivo*

In mice and rats ^{18}F-LW223 rapidly distributed to TSPO expressing tissues, including brain, heart and lung following administration. It was eliminated via both the urinary and hepatobiliary excretion routes (Fig.3.A, Left).

Radiometabolism of ^{18}F-LW223 in rat arterial blood was slow with approximately 62% of the parent compound remaining at 120 min post-injection (Fig.3.A, Middle and Supplemental Fig.6). Less than 12.7% radiometabolites were measured in the brain, heart and lung at 60 and 120 min post-administration (Fig.3.A, Right and Supplemental

Fig.7). The measured parent free fraction in plasma (f_p) was 38.5±7.0% (mean±SEM, n = 5).

Peak SUVs in naive rat brain, heart and lung were 0.83±0.18, 2.51±0.31 and 3.98±0.35 g/mL, respectively. Post-peak uptake, elimination of the radiotracer was faster in the brain and lung compared with the heart (Supplemental Fig.8). Time activity curves were noisier in the sampled LV sub-region relative to whole organ VOIs (Supplemental Fig.8.D-F). ^{18}F-LW223 kinetics in naive rats were blockable (Fig.3.B-C), reversible (Supplemental Fig.9) and could be described by the 2-tissue compartmental model (2TCM, Supplemental Table.4).

In naive mice, the highest %injected dose was in the gut followed by the liver, lung, kidneys, heart, brain, gall bladder, urinary bladder and adrenals. Dosimetry estimates demonstrated that the critical organ was the lower large intestine. The whole-body effective dose was estimated to be 20.5 (male) and 24.5 μSv/MBq (female, Table.1).

^{18}F-LW223 BP_{TC} Allows for Detection of Macrophage-Driven Inflammation in the Hypoperfused Myocardium Following-MI

In non-perfusion-corrected SUV heart images there was an increase in ^{18}F-LW223 signal globally with a lack of signal within the left ventricle (LV) anterior wall (area of the infarct, Fig.4.A, Left) seven days following MI. There was a significant decrease in the measured total volume of distribution (V_T) in the LV anterior wall, i.e. infarct area, in the MI group (Fig.4.A, Middle). V_T and SUV values at pseudo-equilibrium ($SUV_{40\text{-}60}$) in naive and MI animals significantly correlate (Supplemental Fig. 10). However, heart VOIs on their own do not correlate in MI animals suggesting that V_T and SUV are not equally

affected by tissue hypoperfusion induced by the coronary artery ligation. The K_1 was also significantly reduced in the LV anterior wall of the MI group (Fig.4.A, Right and Supplemental Table.4). The measured reduction in all modelling constants was not linear, with k_2 only reducing 1.4 fold *versus* 3.6 fold for K_1 (Supplemental Table.4). The ratio of the constants k_3/k_4 remained unchanged between groups (Supplemental Table.4). Fig.4.B contains examples of parametric images of a left ventricle from the MI group, with the perfusion deficit caused by the ligation of the left anterior descending artery clear in the K_1 image (Left). The BP_{TC} parametric imaging data showed a clear signal mainly within the infarct (Fig.4.B, Middle). Quantification of BP_{TC} between groups demonstrated a significant increase between naive and MI within the LV anterior wall (Fig.4.B, Right). There was no statistically significant changes in measured ^{18}F-LW223 concentration in whole blood following MI (Supplemental Fig.11).

Validation of BP_{TC} was performed by *ex-vivo* analysis of naive and MI hearts and immunofluorescent staining of TSPO and CD68 (Fig.4.C). In the naive and MI heart, the vast majority of TSPO staining (green, cytoplasmic) was found in macrophages which were CD68 positive (red, cytoplasm and cell surface). These markers only occasionally co-localized to the same region of the cell (yellow) due to their sub-cellular distribution. Quantification of TSPO staining revealed a significant increase in the LV anterior wall of the MI group (Fig.4.D, Left), which was also the case for CD68 (Fig.4.D, Middle). TSPO within the global heart and LV anterior wall significantly correlated with CD68 (Fig.4.D, Right). A trend towards a small increase in TSPO and CD68 staining was observed in the remote myocardium (i.e. posterior left ventricle, Supplemental Fig.12). ^{18}F-LW223 autoradiography in these samples also demonstrated an increase in signal within the MI

group (one-way ANOVA, $p<0.05$), although it lacked the statistical power to determine significant regional differences in post-hoc analysis (Supplemental Fig. 13). The localization, and correlation, of TSPO and CD68 within the infarct in *ex vivo* analysis validates the expression pattern seen for ^{18}F-LW223 BP_{TC} *in vivo* (Fig.4.B, Right) and reflects macrophage-driven inflammation in the heart following-MI.

Our simulation work using ideal noise-free conditions shows that the difference between truth BP_{ND} and estimated BP_{ND} is more pronounced for low K_1 values (Supplemental Fig.14, Supplemental Tables 5 to 8). This simulates conditions of severe hypoperfusion, such as those observed during MI. Furthermore, data shows that in areas of low BP_{ND} (e.g. brain), the reduction of K_1 needs to be much higher than in areas of expected high BP_{ND} (e.g. infarct region), in order to impact BP_{ND} measures (Supplemental Fig.14).

^{18}F-LW223 PET Corroborates Existence Of An Inflammatory Heart:Brain Axis in Rats Following-MI

In line with previous observations in mice and humans (*6*), we investigated the existence of a TSPO heart: brain inflammation axis in rats 7 days following MI. There was a significant positive correlation of the ^{18}F-LW223 signal (*in vivo*, Fig.5.A, Left Row and Fig.5.B, Top), TSPO (*ex-vivo* immunofluorescence, Fig.5.A, Middle Row and Fig.5.B, Middle) and CD68 (*ex-vivo* immunofluorescence, Fig.5.A, Middle Row and Fig.5.B, Bottom) expression between the heart and brain of naive and MI rats. *Ex-vivo* TSPO analysis revealed a significant increase following MI within the lateral ventricles of the brain, but no significant change in the global brain, hippocampus, thalamus or cortex

(Supplemental Fig.15). Examples of TSPO and CD68 cellular expression with and without co-localization in the brain are shown in Fig.5.A (right row).

DISCUSSION

The first aim of this study was to develop a novel TSPO ligand that was insensitive to the rs6971 genetic polymorphism *in vitro* using the gold standard human tissue competition binding assays and two types of tissue (brain and heart); which in this case was LW223. Three recently developed PET compounds have also been proposed to be insensitive to the human rs6971 genetic polymorphism: ^{18}F-FEBMP (small pilot autoradiography study, n = 2) (*30*), (*R*)-^{18}F-NEBIFQUINIDE (binding assessed using human thrombocyte membranes) (*31*), and (*R,S*)-^{18}F-GE387 (binding assessed using human embryonic kidney cell lines overexpressing human TSPO wild-type and TSPO A147T) (*32*). Unfortunately, ^{18}F-FEBMP underwent considerable metabolism when assessed in rats, with <10% of the original parent compound found in blood at 30 min post-injection (*30*). *In vivo* kinetic properties in animal models of disease and dosimetry estimates of both (*R*)-^{18}F-NEBIFQUINIDE and (*R,S*)-^{18}F-GE387 are yet to be fully assessed. Meanwhile, our study presents detailed *in vivo* kinetic modelling, target-engagement quantification and animal disease model studies with ^{18}F-LW223. Thus, ^{18}F-LW223 is the most advanced fluorinated TSPO-PET radiotracer with desirable *in vivo* characteristics and insensitivity to the rs6971 polymorphism in human tissue (as opposed to cell lines and blood cells), which is necessary for clinical translation, reported to date.

Our robust translational package reported here with ^{18}F-LW223 is further complemented by detailed *in vivo* characterization. ^{18}F-LW223 has excellent *in vivo*

properties for imaging TSPO non-invasively. While it is not easy to compare to other radiotracers directly due to differences in species and experimental methods, ^{18}F-LW223 had a V_T in the brain of 1.2-2.13 mL/cm^3, which was higher than reported values for ^{11}C-PK11195 (0.6-0.74 mL/cm^3) (*33*) and ^{18}F-GE180 (0.10-0.28 mL/cm^3) (*34*,*35*). This was in line with other promising TSPO radiotracers such as ^{11}C-ER176 (1.6-3.5 mL/cm^3) and ^{18}F-PBR111 (2.22-4.03 mL/cm^3) (*36*,*37*). ^{18}F-LW223 SUV brain values in rats (ranging between 0.5-1.3 mg/mL over time) also compared favourably with ^{11}C-PK11195 (0.6-0.8 mg/mL) (*38*) in the same species. Comparison of ^{18}F-LW223 performance in mapping TSPO in heart and lung is more challenging owing to limited data on previously developed TSPO PET radiotracers outside the brain. Still, ^{18}F-LW223 SUV in rat heart and lung (3.5-4.5 and 3-3.5, respectively) also compared positively with ^{11}C-PK11195 (peak SUV in heart of 5 and in lung of 3) in humans (*39*). Importantly, ^{18}F-LW223 has a considerably high f_p of 38.5% compared to ^{11}C-PBR28 (21%) (*40*) in rats; and ^{11}C-PBR28 (3-11%) (*16*), ^{11}C-PK11195 (1%) (*41*) and ^{11}C-ER176 (3.3%) (*36*) in humans. ^{18}F-LW223 also has an excellent radiometabolic profile (62% parent at 120 min in plasma) which is higher than ^{11}C-PK11195 (c. 40%, (*42*) in the same lower species). The measured radiometabolites in plasma were less lipophilic than the parent compound, suggesting they would have lower brain penetration. This is confirmed by the low fraction of radiometabolites measured in brain tissue and other target organs, which will minimally impact on *in vivo* PET data quantification. ^{18}F-LW223 binding to TSPO *in vivo* was blocked and displaced by PK11195, indicating the specificity of this novel ligand for TSPO. The estimated dosimetry of ^{18}F-LW223 (0.020 mSv/MBq) was also well within typical values for ^{18}F-

labeled radiotracers currently in routine clinical use (e.g. ^{18}F-FDG 0.029 mSv/MBq (*43*)), therefore easing translation to humans.

An additional aim of this study was to develop a novel multi-parametric analysis approach which would allow for accurate quantification of regional TSPO expression within the infarcted myocardium with a single scan paradigm. We utilized dynamic imaging and 2TCM to quantify the different rate kinetics of the ^{18}F-LW223 signal. Traditionally, 2TCM is used to calculate V_T (*19*). Our data demonstrated that the drop in K_1 was severely perturbed within the infarct region to a far greater extent than the other constants, particularly k_2. Due to the imbalanced decrease in movement of radiotracer from the blood into the tissue (K_1) and the reverse (k_2), and the fact during these hypoperfused conditions $K_1 \rightarrow F$, V_T was not able to reflect disease activity accurately. For our high affinity ligand, ^{18}F-LW223, and in the highly hypoperfused and inflamed myocardium, the result is a violation of the Michaelis-Menten free ligand approximation principle. In these circumstances, the Morrison kinetics of tight binding reversible ligands apply (*44*,*45*).

Our reported K_1 values (Supplementary Table.4) were relatively high in the heart and lung but not in the brain, which indicates that the respective PS is also high for ^{18}F-LW223 and thus support the $K_1 \rightarrow F$ assumption. Moreover, our *in vivo* modelling data are also corroborated by *ex vivo* tissue analysis with PET-independent measures of antibody-tagged TSPO immunofluorescence. ^{18}F-LW223 can be classified as a moderately extracted radiotracer if we use ^{15}O-water as a benchmark for high extraction. Therefore, theoretically, for large flows (e.g. healthy myocardium) deviation of apparent K_1 (i.e. flow×extraction) from the flow line of identity would be more pronounced than low flows

(e.g. infarcted region) (*46*). This is in fact similar and expected behavior to routinely used SPECT or PET myocardial perfusion agents (e.g. ^{99m}Tc-Sestamibi or ^{18}F-Flurpiridaz) (*47*).

Previously this hemodynamic change following MI has been corrected using an additional SPECT scan (*6*), resulting in an increased cost and patient burden. Here we derived BP_{TC} as a new outcome measure for quantification of the TSPO PET signal using a single-scan protocol. Currently, we make use of the gold standard invasive arterial sampling for data quantification, although this is not always practical in a clinical setting. With the validation of BP_{TC} using *ex-vivo* histology, clinical translation can now take place using simplified non-invasive image derived input function (IDIF) to derive robust outcome measures in line with our previously reported findings (*48*).

Our simulation work using ideal noise-free conditions shows that in areas of low BP_{ND} (a proxy for TSPO brain uptake), the reduction of K_1 needs to be much higher than in areas of expected high BP_{ND} (a proxy for TSPO heart uptake) to impact BP_{ND} measures. Sander *et al.* have recently reported that large K_1 and small k_2 values (i.e. large volume of distribution, V_D) are most sensitive to changes in blood flow (*49*). This is in line with our data and point out important differences when assessing radiotracer binding in the heart (where V_D is high) versus the brain (where V_D is low). Therefore, even though minor BP_{ND} changes in the brain were reported by Sander *et al.* due to cerebral blood flow increases up to 100% mid-scan, these observations might not translate directly to other organs and hypoperfusion scenarios as oppose to hyperperfusion. In particular, studies have shown that following MI, vascular remodelling includes regional vasodilation, vasoconstriction, or pruning. All of these have been shown to impact on microvascular

conductivity (*50*); which could contribute to imbalanced K_1 versus k_2 changes beyond flow changes.

Previous studies using chemokine receptor type 4 (CXCR-4) radiotracers, an alternative inflammatory target, have shown that the highest radiotracer signal was detected in areas of infarct at 3 days post-MI without perfusion correction (*51*,*52*). Differences between these studies and ours may be due to the difference in target, size of radiotracer molecule, experimental model and time point assessed. These last two points result in considerable differences in blood flow, haemodynamic responses and tissue remodelling stages which will impact imaging outcomes.

In the rat MI model used in this study, we demonstrated that the majority of TSPO expression (BP_{TC}) was within the infarct region of the MI cohort, which was in agreement with *ex-vivo* analysis. However, it should be noted that in non-infarcted myocardium in other MI/cardiomyopathy models of heart failure, there is significant TSPO expression, indicating that TSPO may have a wider role in the failing heart (*53*,*54*).

A limitation in our study is that we only assessed one time point in our MI study. Follow up studies with longitudinal TSPO imaging following MI in rats are being planned which will be necessary to robustly assess the transient nature of inflammation and this molecular target. In addition, it is currently not clear whether targeting TSPO in macrophages is selective for M1 or M2 phenotypes, with previous evidence being conflicted on this aspect (*6*,*55*,*56*). This is something which we also plan to address in our follow-up studies in addition to selectivity of 18F-LW223 for different leukocyte subpopulations as has been previously carried out (*6*). Another limitation of our study is that we have only carried out radiometabolite analysis of ^{18}F-LW223 in naive rats. Our

data suggests there are no significant differences in radioactive concentration in blood of naïve versus MI animals, however, it is possible that the metabolite profile of ^{18}F-LW223 changes during MI and this could affect the PET outcome measures.

With the advent of total-body PET clinical scanners (*57*), assessment of multi-organ responses to disease will become increasingly important in medical research. This is attractive for TSPO-PET studies, given that TSPO has served as a marker of regional tissue inflammation in pathologies throughout the body (*4*,*6*–*10*). In this study, we observed a significant positive correlation between the brain and heart following MI, which was detected by ^{18}F-LW223 PET imaging *in vivo*, and TSPO and CD68 staining *ex-vivo*. Additionally, our *ex-vivo* results demonstrated a trend towards increased TSPO expression staining in the whole brain post-MI, albeit without reaching significance. The degree of the change was small, and similar to the change previously reported by Thackeray *et al.* (*6*). However, at a regional level there was increased expression in TSPO within the lateral ventricles. It is possible that the increased signal in the brain is due to blood-brain-barrier hyper-permeability and dysfunction of the blood-cerebrospinal fluid system, which exist to preserve central nervous system homeostasis (*58*). This is corroborated by the increase in TSPO expression we observed in the lateral ventricles and agrees with previous studies demonstrating the role of the choroid plexus in the recruitment of macrophages at distant sites (*59*,*60*). At a cellular level, although some TSPO expression co-localized with the CD68 marker in the brain, there were cells positive for TSPO that lacked co-expression with CD68. This is to be expected, as TSPO is expressed in a number of brain cell types (*61*). Overall, our results with ^{18}F-LW223 PET in this rat model of MI corroborate the findings by Thackeray *et al.* in mice and humans,

thus echoing the importance of integrative systems biology analysis in PET studies (*6*). The clinical importance of the heart:brain axis following MI is not yet clear and should be investigated further.

In conclusion, we have developed a novel TSPO radiotracer which is not susceptible to the rs6971 human genetic polymorphism in addition to an original multi-parametric analysis approach. These tools now warrant further investigation and translation in the fields of cardiology and neurology.

ACKNOWLEDGMENTS

This work was funded by the British Heart Foundation (PG/16/12/32022 and PG/17/83/33370) and the Engineering and Physical Sciences Research Council (EPSRC Impact Acceleration Awards, EP/K5039031 and EP/R511705/1). The British Heart Foundation is greatly acknowledged for providing funding towards establishment of the preclinical PET/CT laboratory at the University of Edinburgh (RE/13/3/30183) and radiometabolite laboratories (RG/16/10/32375). AAST and TW are funded by the British Heart Foundation (RG/16/10/32375, FS/19/34/34354). MGM is funded by the British Heart Foundation (PG/16/12/32022, PG/17/83/33370 and RG/16/10/32375) and ASt by the British Heart foundation (RE/13/3/30183). DEN is funded by the British Heart Foundation (CH/09/002, RG/16/10/32375, RE/18/5/34216) and is the recipient of a Wellcome Trust Senior Investigator Award (WT103782AIA). CA-C and CL are supported by the Edinburgh Preclinical Imaging and Edinburgh Imaging core facilities, respectively. The authors would like to thank and acknowledge the Edinburgh Brain and Tissue Bank for providing the tissues used in this study (full tissue list in Sup.Table.2). The authors

would also like to thank Lee Murphy, William Hawkins and Sarah McCafferty from the Genetics Core at the Edinburgh Clinical Research Facility for their extremely valuable technical support with genotyping of the human tissue samples. The research team acknowledges the financial support of NHS Research Scotland (NRS), through Edinburgh Clinical Research Facility.

Disclosure

The authors declare submission of a patent application number GB1810312.7. No other potential conflicts of interest relevant to this article exist.

Key Points

QUESTION

Is our newly developed TSPO radiotracer, ^{18}F-LW223¸ able to detect macrophage-driven inflammation following myocardial infarction while being suitable for clinical translation and not affected by the rs6971 human genetic polymorphism?

PERTINENT FINDINGS:

Binding of ^{18}F-LW223 to TSPO in human brain and heart in vitro assays demonstrated that it was not susceptible to the rs6971 genetic polymorphism; while the preclinical in vivo characterisation indicated that ^{18}F-LW223 is specific, has favourable metabolism and a dosimetry profile suitable for translation. In a preclinical rat myocardial infarction model ^{18}F-LW223 BP_{TC} was significantly increased within the infarct relative to naive myocardium, which mirrored the pattern of macrophage expression in these animals detected by ex-vivo immunofluorescent staining.

IMPLICATIONS FOR PATIENT CARE:

As ^{18}F-LW223 is not affected by the rs6971 human genetic polymorphism, and has excellent in vivo characteristics, it is a prime candidate for further clinical translation which could ultimately lead to the development of a prognostic tool for use in patients following myocardial infarction.

REFERENCES

1. Organisation WH. Cardiovascular diseases (CVDs) Fact Sheet. Accessed on 6th December 2018. https://www.who.int/news-room/fact-sheets/detail/cardiovascular-diseases-(cvds).

2. Ong SB, Hernández-Reséndiz S, Crespo-Avilan GE, et al. Inflammation following acute myocardial infarction: Multiple players, dynamic roles, and novel therapeutic opportunities. *Pharmacol Ther*. 2018;186:73-87.

3. Lacapère JJ, Papadopoulos V. Peripheral-type benzodiazepine receptor: Structure and function of a cholesterol-binding protein in steroid and bile acid biosynthesis. *Steroids*. 2003;68:569-585.

4. Bird JLE, Izquierdo-Garcia D, Davies JR, et al. Evaluation of translocator protein quantification as a tool for characterising macrophage burden in human carotid atherosclerosis. *Atherosclerosis*. 2010;210:388-391.

5. Cosenza-Nashat M, Zhao ML, Suh HS, et al. Expression of the translocator protein of 18 kDa by microglia, macrophages and astrocytes based on immunohistochemical localization in abnormal human brain. *Neuropathol Appl Neurobiol*. 2009;35:306-328.

6. Thackeray JT, Hupe HC, Wang Y, et al. Myocardial inflammation predicts remodeling and neuroinflammation after myocardial infarction. *J Am Coll Cardiol*. 2018;71:263-275.

7. Gerhard A. TSPO imaging in parkinsonian disorders. *Clin Transl Imaging*. 2016;4:183-190.

8. Repalli J. Translocator protein (TSPO) role in aging and alzheimer's disease. *Curr Aging Sci*. 2015;7:168-175.

9. Abid KA, Sobowale OA, Parkes LM, et al. Assessing inflammation in acute intracerebral hemorrhage with PK11195 PET and dynamic contrast-enhanced MRI. *J Neuroimaging*. 2018;28:158-161.

10. Gulyas B, Toth M, Vas A, et al. Visualising neuroinflammation in post-stroke patients: A comparative PET study with the TSPO molecular imaging biomarkers [11C]PK11195 and [11C]vinpocetine. *Curr Radiopharm*. 2012;5:19-28.

11. Charbonneau P, Syrota A, Crouzel C, et al. Peripheral-type benzodiazepine receptors in the living heart characterized by positron emission tomography. *Circulation*. 1986;73:476-483.

12. Chauveau F, Boutin H, Van Camp N, et al. Nuclear imaging of neuroinflammation: A comprehensive review of [11C]PK11195 challengers. *Eur J Nucl Med Mol Imaging*. 2008;35:2304-2319.

13. Owen DR, Yeo AJ, Gunn RN, et al. An 18-kDa translocator protein (TSPO) polymorphism explains differences in binding affinity of the PET radioligand PBR28. *J Cereb Blood Flow Metab*. 2012;32:1-5.

14. Stevenson L, Tavares AAS, Brunet A, et al. New iodinated quinoline-2-carboxamides for SPECT imaging of the translocator protein. *Bioorg Med Chem Lett*. 2010;20:954-957.

15. Cappelli A, Anzini M, Vomero S, et al. Mapping the peripheral benzodiazepine receptor binding site by conformationally restrained derivatives of 1-(2-

chlorophenyl)-N-methyl-N-(1- methylpropyl)-3-isoquinolinecarboxamide (PK11195). *J Med Chem*. 1997;40:2910-2921.

16. Owen DRJ, Gunn RN, Rabiner EA, et al. Mixed-affinity binding in humans with 18-kDa translocator protein ligands. *J Nucl Med*. 2011;52:24-32.

17. Warnock G, Bahri MA, Goblet D, et al. Use of a beta microprobe system to measure arterial input function in PET via an arteriovenous shunt in rats. *EJNMMI Res*. 2011;1:1-11.

18. Spath NB, Lilburn DML, Gray GA, et al. Manganese-enhanced T1 mapping in the myocardium of normal and infarcted hearts. *Contrast Media Mol Imaging*. 2018;2018:1-13.

19. Innis RB, Cunningham VJ, Delforge J, et al. Consensus nomenclature for in vivo imaging of reversibly binding radioligands. *J Cereb Blood Flow Metab*. 2007;27:1533-1539.

20. Stabin MG, Sparks RB, Crowe E. OLINDA/EXM: The second-generation personal computer software for internal dose assessment in nuclear medicine. *J Nucl Med*. 2005;46:1023-1027.

21. Tavares AAS, Caillé F, Barret O, et al. Whole-body biodistribution and dosimetry estimates of a novel radiotracer for imaging of serotonin 4 receptors in brain: [18F]MNI-698. *Nucl Med Biol*. 2014;41:432-439.

22. Khanuja B, Cheah YC, Hunt M, et al. Lith1, a major gene affecting cholesterol gallstone formation among inbred strains of mice. *Proc Natl Acad Sci*. 1995;92:7729-7733.

23. Bielohuby M, Herbach N, Wanke R, et al. Growth analysis of the mouse adrenal gland from weaning to adulthood: time- and gender-dependent alterations of cell size and number in the cortical compartment. *Am J Physiol Metab*. 2007;293:E139-E146.

24. Stabin MG, Peterson TE, Holburn GE, et al. Voxel-based mouse and rat models for internal dose calculations. *J Nucl Med*. 2006;47:655-9.

25. Hindorf C, Ljungberg M, Strand S-E. Evaluation of parameters influencing S values in mouse dosimetry. *J Nucl Med*. 2004;45:1960-5.

26. Hui TE, Fisher DR, Kuhn JA, et al. A mouse model for calculating cross-organ beta doses from yttrium-90-labeled immunoconjugates. *Cancer*. 1994;73:951-957.

27. Tóth ZE, Mezey É. Simultaneous visualization of multiple antigens with tyramide signal amplification using antibodies from the same species. *J Histochem Cytochem*. 2007;55:545-554.

28. Cheng Y-C, Prusoff WH. Relationship between the inhibition constant (KI) and the concentration of inhibitor which causes 50 per cent inhibition (I50) of an enzymatic reaction. *Biochem Pharmacol*. 1973;22:3099-3108.

29. Blair A, Zmuda F, Malviya G, et al. A novel F-18-labelled high affinity agent for PET imaging of the translocator protein. *Chem Sci*. 2015;6:4772-4777.

30. Tiwari AK, Ji B, Yui J, et al. [18F]FEBMP: Positron emission tomography imaging of TSPO in a model of neuroinflammation in rats, and in vitro autoradiograms of the human brain. *Theranostics*. 2015;5:961-969.

31. Berroterán-Infante N, Kalina T, Fetty L, et al. (R)-[18 F]NEBIFQUINIDE: A

promising new PET tracer for TSPO imaging. *Eur J Med Chem*. 2019;176:410-418.

32. Zanotti-Fregonara P, Pascual B, Rizzo G, et al. Head-to-head comparison of 11C-PBR28 and 18F-GE180 for quantification of the translocator protein in the human brain. *J Nucl Med*. 2018;59:1260-1266.

33. Kobayashi M, Jiang T, Telu S, et al. 11C-DPA-713 has much greater specific binding to translocator protein 18 kDa (TSPO) in human brain than11C-(R)-PK11195. *J Cereb Blood Flow Metab*. 2018;38:393-403.

34. Fan Z, Calsolaro V, Atkinson RA, et al. Flutriciclamide (18F-GE180) PET: First-in-human PET study of novel third-generation in vivo marker of human translocator protein. *J Nucl Med*. 2016;57:1753-1759.

35. Feeney C, Scott G, Raffel J, et al. Kinetic analysis of the translocator protein positron emission tomography ligand [18F]GE-180 in the human brain. *Eur J Nucl Med Mol Imaging*. 2016;43:2201-2210.

36. Ikawa M, Lohith TG, Shrestha S, et al. 11 C-ER176, A radioligand for 18-kDa translocator protein, has adequate sensitivity to robustly image all three affinity genotypes in human brain. *J Nucl Med*. 2017;58:320-325.

37. Guo Q, Colasanti A, Owen DR, et al. Quantification of the specific translocator protein signal of 18F-PBR111 in healthy humans: A genetic polymorphism effect on in vivo binding. *J Nucl Med*. 2013;54:1915-1923.

38. Yankam Njiwa J, Costes N, Bouillot C, et al. Quantitative longitudinal imaging of activated microglia as a marker of inflammation in the pilocarpine rat model of

epilepsy using [11C]-(R)-PK11195 PET and MRI. *J Cereb Blood Flow Metab*. 2017;37:1251-1263.

39. Kreisl WC, Fujita M, Fujimura Y, et al. Comparison of [11C]-(R)-PK 11195 and [11C]PBR28, two radioligands for translocator protein (18 kDa) in human and monkey: Implications for positron emission tomographic imaging of this inflammation biomarker. *Neuroimage*. 2010;49:2924-2932.

40. Walker MD, Dinelle K, Kornelsen R, et al. [11C] PBR28 PET imaging is sensitive to neuroinflammation in the aged rat. *J Cereb Blood Flow Metab*. 2015;35:1331-1338.

41. Endres CJ, Pomper MG, James M, et al. Initial evaluation of 11C-DPA-713, a novel TSPO PET ligand, in humans. *J Nucl Med*. 2009;50:1276-82.

42. Parente A, Feltes PK, Vallez Garcia D, et al. Pharmacokinetic Analysis of 11C-PBR28 in the Rat Model of Herpes Encephalitis: Comparison with (R)-11C-PK11195. *J Nucl Med*. 2016;57:785-791.

43. Deloar HM, Fujiwara T, Shidahara M, et al. Estimation of absorbed dose for 2-[F-18]fluoro-2-deoxy-D-glucose using whole-body positron emission tomography and magnetic resonance imaging. *Eur J Nucl Med*. 1998;25:565-574.

44. Morrison JF. Kinetics of the reversible inhibition of enzyme-catalysed reactions by tight-binding inhibitors. *Biochim Biophys Acta - Enzymol*. 1969;185:269-286.

45. Williams JW, Morrison JF. [17] The kinetics of reversible tight-binding inhibition. In: Methods in Enzymology. Vol 63. ; 1979:437-467.

46. Morris ED, Endres CJ, Schmidt KC, et al. Kinetic modeling in positron emission

tomography. In: Emission Tomography. Elsevier; 2004:499-540.

47. Sogbein OO, Pelletier-Galarneau M, Schindler TH, et al. New SPECT and PET radiopharmaceuticals for imaging cardiovascular disease. *Biomed Res Int*. 2014;2014:1-24.

48. MacAskill MG, Walton T, Williams L, et al. Kinetic modelling and quantification bias in small animal PET studies with [18F]AB5186, a novel 18 kDa translocator protein radiotracer. *PLoS One*. 2019;14:e0217515.

49. Sander CY, Mandeville JB, Wey H-Y, et al. Effects of flow changes on radiotracer binding: Simultaneous measurement of neuroreceptor binding and cerebral blood flow modulation. *J Cereb Blood Flow Metab*. 2019;39:131-146.

50. Gkontra P, El-Bouri WK, Norton K, et al. Dynamic changes in microvascular flow conductivity and perfusion after myocardial infarction shown by image-based modeling. *J Am Heart Assoc*. 2019;8.

51. Thackeray JT, Derlin T, Haghikia A, et al. Molecular imaging of the chemokine receptor CXCR4 after acute myocardial infarction. *JACC Cardiovasc Imaging*. 2015;8:1417-1426.

52. Rischpler C, Nekolla SG, Kossmann H, et al. Upregulated myocardial CXCR4-expression after myocardial infarction assessed by simultaneous GA-68 pentixafor PET/MRI. *J Nucl Cardiol*. 2016;23:131-133.

53. Borchert T, Hess A, Lukačević M, et al. Angiotensin-converting enzyme inhibitor treatment early after myocardial infarction attenuates acute cardiac and neuroinflammation without effect on chronic neuroinflammation. *Eur J Nucl Med*

Mol Imaging. 2020;47:1757-1768.

54. Thai PN, Daugherty DJ, Frederich BJ, et al. Cardiac-specific conditional knockout of the 18-kDa mitochondrial translocator protein protects from pressure overload induced heart failure. *Sci Rep*. 2018;8:1-17.

55. Narayan N, Mandhair H, Smyth E, et al. The macrophage marker translocator protein (TSPO) is down-regulated on pro-inflammatory 'M1' human macrophages. *PLoS One*. 2017;12:1-19.

56. Narayan N, Owen DR, Mandhair H, et al. Translocator protein as an imaging marker of macrophage and stromal activation in rheumatoid arthritis pannus. *J Nucl Med*. 2018;59:1125-1132.

57. Cherry SR, Jones T, Karp JS, et al. Total-body PET: Maximizing sensitivity to create new opportunities for clinical research and patient care. *J Nucl Med*. 2018;59:3-12.

58. Ghersi-Egea JF, Strazielle N, Catala M, et al. Molecular anatomy and functions of the choroidal blood-cerebrospinal fluid barrier in health and disease. *Acta Neuropathol*. 2018;135:337-361.

59. Shechter R, Miller O, Yovel G, et al. Recruitment of beneficial M2 macrophages to injured spinal cord is orchestrated by remote brain choroid plexus. *Immunity*. 2013;38:555-569.

60. Dani N, Herbst RH, Habib N, et al. A cellular and spatial map of the choroid plexus across brain ventricles and ages. *bioRxiv*. January 2019:627539.

61. Betlazar C, Harrison-Brown M, Middleton R, et al. Cellular sources and regional

variations in the expression of the neuroinflammatory marker translocator protein (TSPO) in the normal brain. *Int J Mol Sci*. 2018;19:2707.

Figures

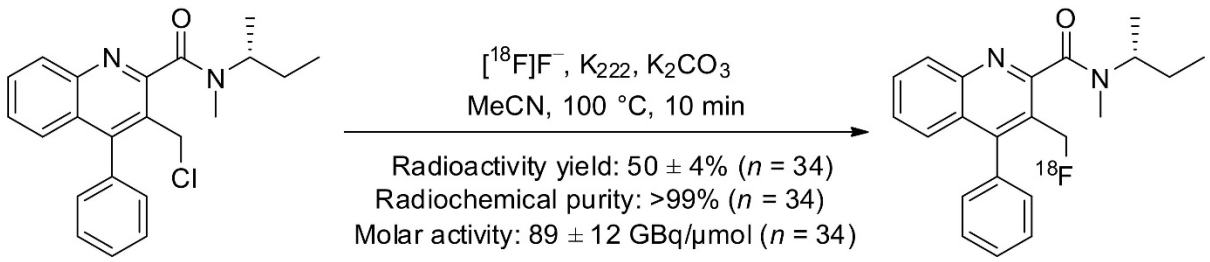

Figure 1. Radiosynthesis of ^{18}F-LW223. Data shown as the mean± SEM.

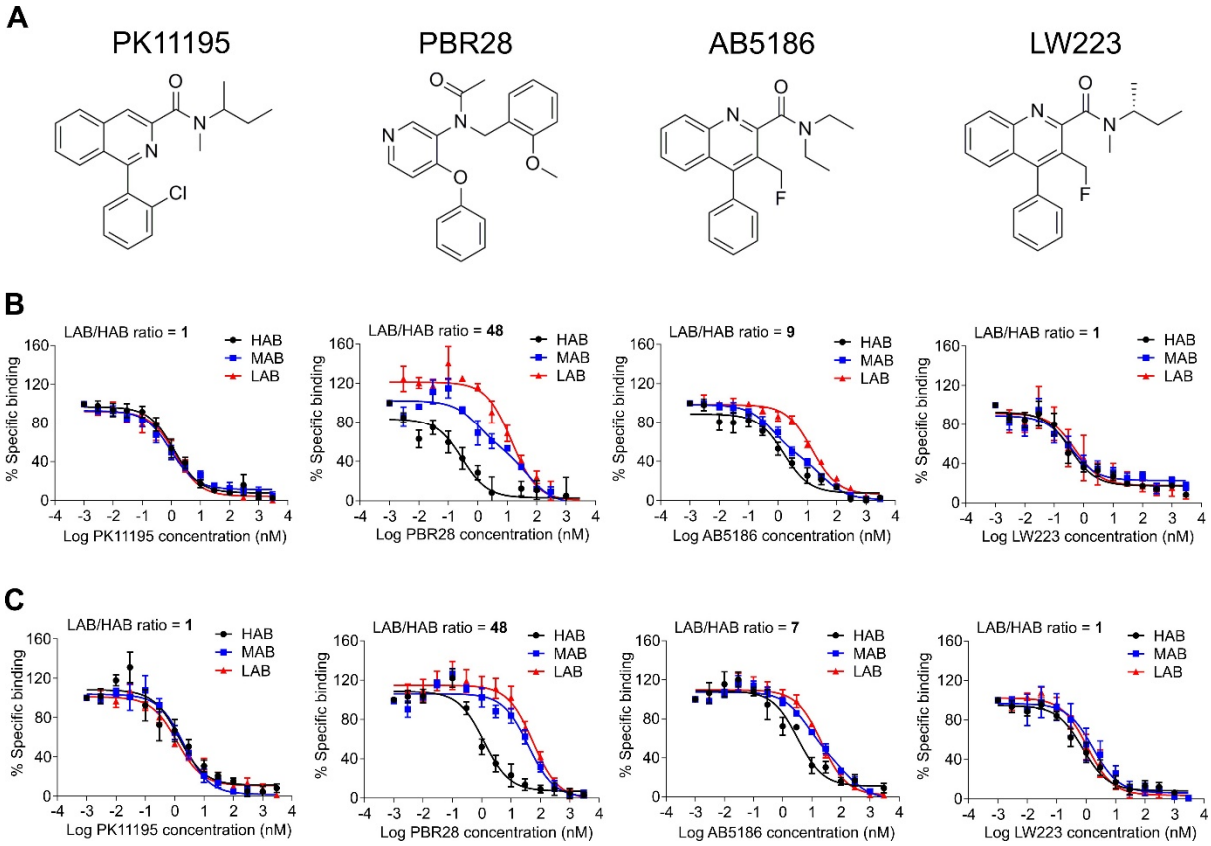

Figure 2. LW223 binding to TSPO is not affected by the human rs6971 genetic polymorphism. A) Chemical structures of established (PK11195, PBR28) and novel (AB5186, LW223) TSPO ligands investigated. **B)** Competition binding assays using the above TSPO ligands in human brain homogenates genotyped and grouped as HAB, MAB and LAB. PK11195 HAB *n* = 6, MAB=8, LAB=4, PBR28 HAB *n* = 4, MAB (two-site fitting)=5, LAB=4, AB5186 HAB *n* = 6, MAB (two-site fitting)=6, LAB=5 and LW223 HAB *n* = 5, MAB=5, LAB=4. Only PK11195 and LW223 were not affected by the polymorphism, which is also demonstrated in **C)** human heart homogenates. PK11195 HAB *n* = 4, MAB=5, LAB=4, PBR28 HAB *n* = 4, MAB=5, LAB=4, AB5186 HAB *n* = 4, MAB=5 (two-site fitting), LAB=4 and LW223 HAB *n* = 5, MAB=5, LAB=4.

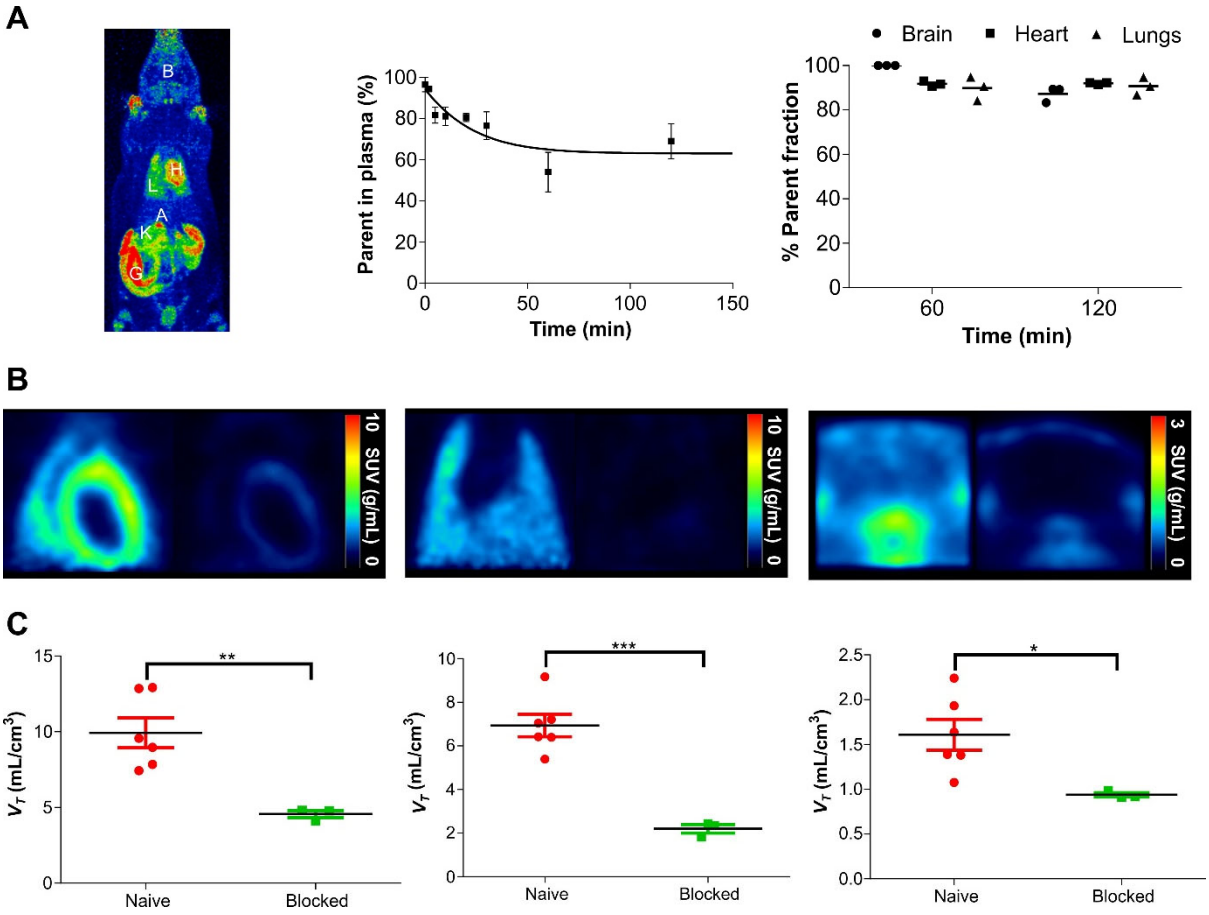

Figure 3. ^{18}F-LW223, assessed in naive rats, has a favorable metabolic profile and specifically targets TSPO *in vivo*. A) Left: Maximum intensity projection of an ^{18}F-LW223 PET scan in a naive rat showing the major uptake organs, B=brain, L=lung, H=heart, G=gut, A=adrenal glands, K=kidney. Middle: Metabolism of ^{18}F-LW223 within rat blood showing a high percentage of parent radiotracer within plasma up to 2 hours post injection, *n* = 3 per time point. Right: Percentage of parent radiotracer within different tissues demonstrating a low level of contaminating radiometabolites, *n* = 3. **B)** SUV images of the rat heart (Left), lung (Middle) and brain (Right) at baseline (left panel) and under TSPO blockade using the prototypical TSPO ligand PK11195 (1 mg/kg, right panel) demonstrating the specificity of ^{18}F-LW223 for this target. SUV PET images were filtered using a Gaussian 1×1×1 mm filter. **C)** Total distribution volume (V_T) within the heart (Left)

lung (Middle) and brain (Right) of naive and TSPO-blocked rats. Results represent the mean±SEM, naive *n* = 6, blocked *n* = 3, *=p<0.05, **=p≤0.01, ***=p≤0.001 using an unpaired t-test.

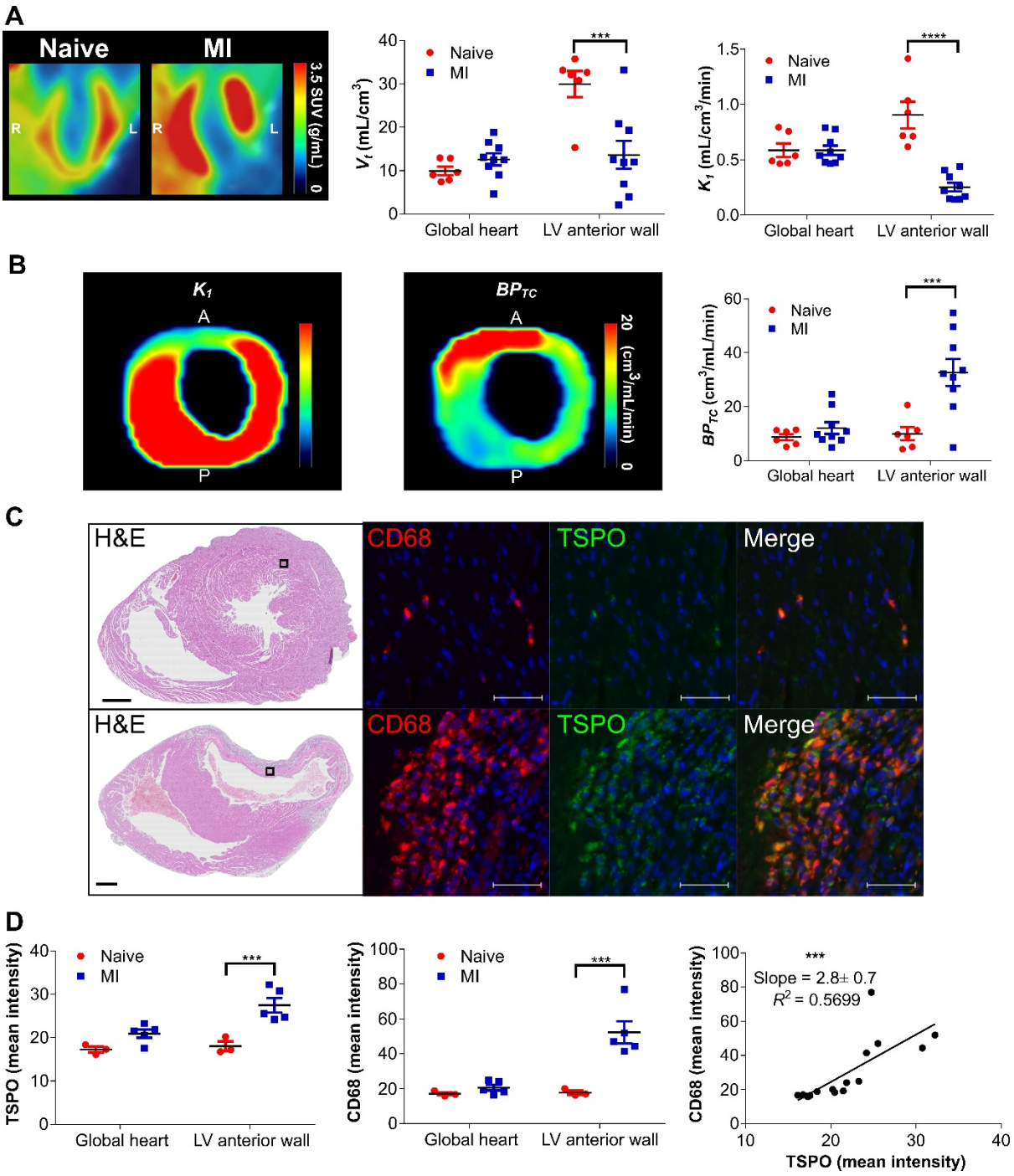

Figure 4. ^{18}F-LW223 PET with *BP_{TC}* quantification detects macrophage-driven inflammation within the heart 7 days post-MI without the need for an additional perfusion scan. A) Left: A long axis representative SUV image of the heart in naive and MI rats showing increased global uptake and lack of signal within the left ventricle (LV)

anterior wall due to the MI-mediated reduction in perfusion. R=right side, L=left side. Images were filtered using a Gaussian 1×1×1 mm filter. Middle: Non-perfusion corrected volume of distribution (V_T) measurements within the global heart and LV anterior wall which was the site of infarct. Right: The rate constant K_1 acts as a surrogate marker of perfusion and is reduced within the LV anterior wall. **B)** Left: Representative K_1 and transfer corrected BP_{ND} (BP_{TC}) images (Middle) of the left ventricle of an MI rat demonstrating the true TSPO signal across the heart. A=anterior and P=posterior. Right: BP_{TC} values across the global heart and LV anterior wall demonstrating that the majority of TSPO is expressed within the infarct. **C)** Representative histology examples of hearts from a naive (top row) and MI (bottom row) rat. The left panel is a H&E overview (scale bar=1000 μm) containing a box which indicates the position of the CD68 (macrophage marker) and TSPO examples (scale bar= 50 μm) demonstrating the specificity of TSPO for macrophages which are mostly present within the infarct. **D)** Left: Quantification of the TSPO immunofluorescent stain indicating that the majority of the signal is present within the LV anterior wall, as is also the case with the CD68 quantification (Middle). Right: Comparison of TSPO and CD68 indicates a significant correlation within the heart. Results represent the mean±SEM, n = 6 for naive, n = 5 for MI. **=p≤0.01, ***=p≤0.001 and ****= p≤0.0001 using a two-way ANOVA with post-hoc Sidak for naive vs. MI apart from the correlation analysis which used Pearson correlation.

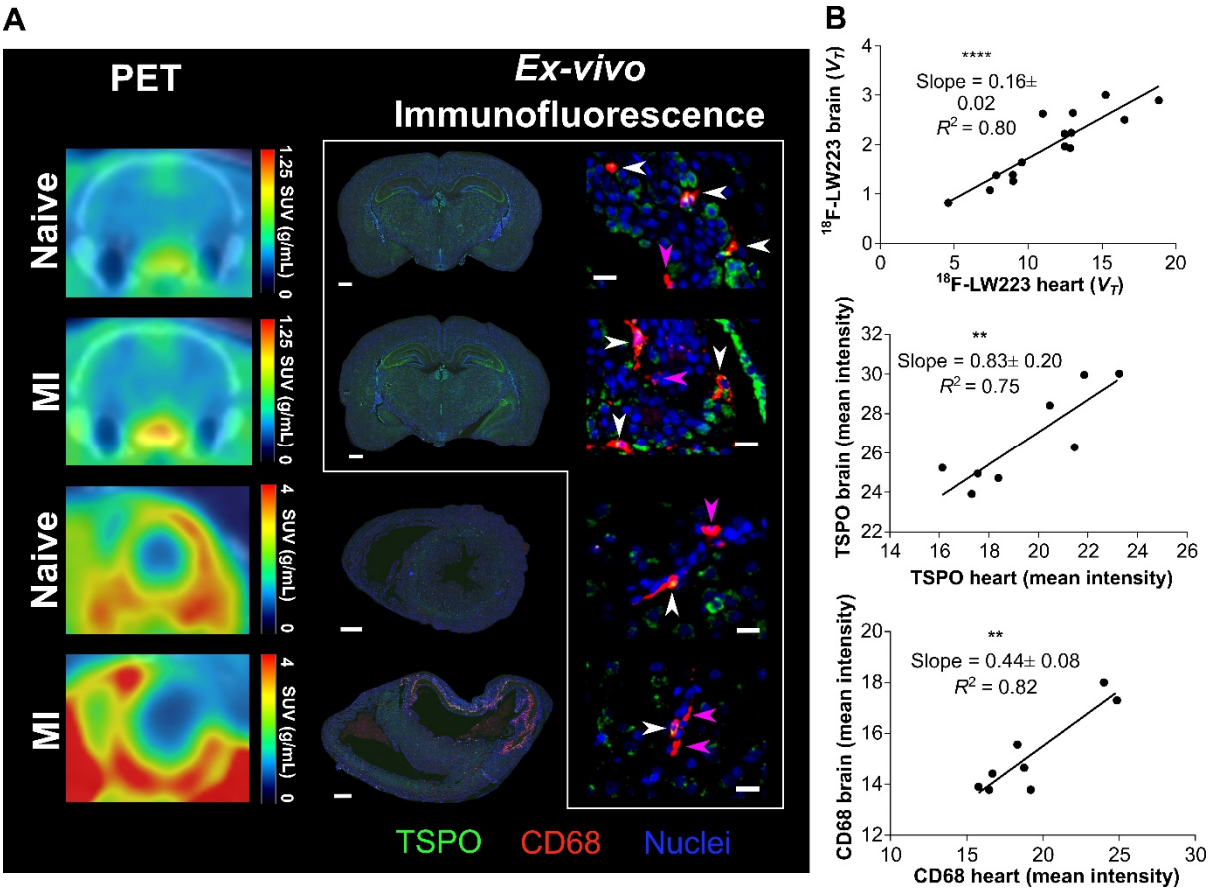

Figure 5. The heart: brain axis in health and following myocardial infarction. A) Left Row: Representative ^{18}F-LW223 brain (coronal section) and heart (short axis) PET/CT images of naive and MI rats. Middle Row: CD68 (red) and TSPO (green) immunofluorescence within the same animals, scale bar=1000 μm. Right Row: Regional brain immunofluorescence within the lateral ventricles of naive (top) and MI (second top). Regional brain immunofluorescence within the thalamus of naive (second to bottom) and MI (bottom), scale bar=20 μm. White arrow denotes cells which are both CD68 and TSPO positive, the pink arrow indicates cells positive only for CD68. Cells positive only for TSPO were abundant and are not specifically denoted. **B)** Top: Comparison of ^{18}F-LW223 V_T in the heart and brain of naive and MI rats showing a strong correlation, as is also the

case for TSPO (Middle) and CD68 (Bottom). **=p≤0.01, **=p≤0.0001 using Pearson correlation.

	Estimated Absorbed Dose $\times 10^{-2}$ mGy/MBq	
Target Organ	**Male**	**Female**
Adrenals	2.22	3.67
Brain	0.59	0.56
Breasts	0.72	0.86
Gallbladder Wall	2.01	2.46
LLI Wall	7.82	9.26
Small Intestine	1.11	1.30
Stomach Wall	0.94	1.15
ULI Wall	1.00	1.24
Heart Wall	2.03	1.89
Kidneys	1.57	1.54
Liver	1.30	1.95
Lung	3.10	3.31
Muscle	0.80	0.98
Ovaries	-	1.66
Pancreas	1.03	1.26
Red Marrow	0.82	0.98
Osteogenic Cells	1.20	1.52
Skin	0.61	0.74
Spleen	0.91	1.11
Testes	0.77	-
Thymus	0.90	1.07
Thyroid	0.79	0.89
Urinary Bladder Wall	1.16	1.48
Uterus	-	1.29
Total Body	0.89	1.07
Effective Dose (mSv/MBq)	0.02	0.02

Table 1. Estimated ^{18}F-LW223 radiation dose for humans is within acceptable limits for future clinical use. LLI=lower large intestine, ULI=upper large intestine, male *n* = 8, female *n* = 5.

SUPPLEMENTAL METHODS

Organic Chemistry

All reagents and starting materials were obtained from commercial sources and used as received. All dry solvents were purified using a PureSolv 500 MD solvent purification system. All reactions were performed under argon unless otherwise stated. Brine is defined as a saturated solution of aqueous sodium chloride. Flash column chromatography was carried out using Fisher Matrix silica 60. Macherey–Nagel aluminium–backed plates pre–coated with silica gel 60 (UV254) were used for thin layer chromatography and were visualized using UV light. ^{1}H NMR and ^{13}C NMR spectra were recorded on a Bruker DPX 400 spectrometer or Bruker 500 spectrometer with chemical shift values in ppm relative to tetramethylsilane (δ_H 0.00 and δ_C 0.0) or residual chloroform (δ_H 7.26 and δ_C 77.2) as the standard. ^{1}H and ^{13}C assignments are based on two-dimensional COSY and DEPT experiments, respectively. Infrared spectra were recorded on a JASCO FTIR 410 spectrometer. Mass spectra were recorded using electron impact, chemical ionization or fast atom bombardment techniques. HRMS spectra were recorded using a dual-focusing magnetic analyzer mass spectrometer. Melting points were determined on a Gallenkamp melting point apparatus. Chiral High Performance Liquid Chromatography (HPLC) methods were calibrated with the corresponding racemic mixtures. 3-Methyl-4-phenylquinoline-2-carboxylic acid was prepared as previously reported *(14)*.

(*R*)-(*N-sec*-Butyl)-3-methyl-4-phenylquinoline-2-carboxamide

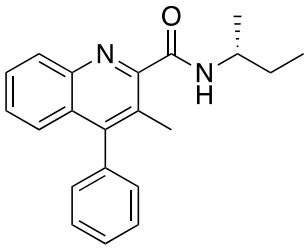

To a solution of 3-methyl-4-phenylquinoline-2-carboxylic acid (2.54 g, 9.65 mmol) in anhydrous *N*,*N*-dimethylformamide (250 mL) was added *O*-(benzotriazol-1-yl)-*N*,*N*,*N*′,*N*′-tetramethyluronium hexafluorophosphate (5.49 g, 14.5 mmol) and *N*,*N*-diisopropylethylamine (3.40 mL, 19.3 mmol). The reaction mixture was stirred at room temperature for 0.5 h before the addition of (*R*)-(−)-*sec*-butylamine (1.10 mL, 10.6 mmol) and then heated to 40 °C for 4 h. The reaction mixture was cooled to room temperature, diluted with ethyl acetate (300 mL) and washed with water (3 × 200 mL) and brine (200 mL). The organic layer was dried ($MgSO_4$), filtered and concentrated *in vacuo* to give a brown oil. Purification by flash column chromatography (petroleum ether/ethyl acetate, 4:1) gave (*R*)-(*N*-*sec*-butyl)-3-methyl-4-phenylquinoline-2-carboxamide as a white solid (2.81 g, 91%). Mp 152–154 °C (lit.*(15)* mp 157–158 °C); IR (KBr) 3287 (NH), 2968 (CH), 1641 (CO), 1539, 1448, 1157, 761 cm^{-1}; $[\alpha]_D^{25}$ –26.7 (*c* 1.0, $CHCl_3$); ^1H NMR (400 MHz, $CDCl_3$) δ 1.03 (3H, t, *J* = 7.4 Hz, $CHCH_2CH_3$), 1.33 (3H, d, *J* = 6.6 Hz, $CHCH_3$), 1.61–1.75 (2H, m, CH_2CH_3), 2.56 (3H, s, 3-CH_3), 4.08–4.20 (1H, m, $CHCH_3$), 7.21–7.25 (2H, m, ArH), 7.35 (1H, d, *J* = 8.3 Hz, ArH), 7.40–7.55 (4H, m, ArH), 7.65 (1H, ddd, *J* = 8.3, 6.8, 1.4 Hz, ArH), 7.90 (1H, d, *J* = 8.3 Hz, NH), 8.09 (1H, d, *J* = 8.3 Hz, ArH); ^{13}C NMR (101 MHz, $CDCl_3$) δ 10.6 (CH_3), 17.6 (CH_3), 20.5 (CH_3), 29.9 (CH_2), 46.8 (CH), 126.1 (CH), 127.5 (CH), 127.9 (CH), 128.6 (C), 128.6 (2 × CH), 128.7 (CH and C), 129.3 (2 × CH), 129.5 (CH), 137.3 (C), 144.7 (C), 149.5 (C), 150.1 (C), 166.2 (C); MS (CI) *m/z* 319

(M+H$^+$, 100%), 220 (19), 202 (5), 148 (6), 113 (16), 85 (77); HRMS (CI) calcd for $C_{21}H_{23}N_2O$ (M+H$^+$), 319.1810, found 319.1809.

(*R*)-(*N*-*sec*-Butyl)-*N*-methyl-3-methyl-4-phenylquinoline-2-carboxamide

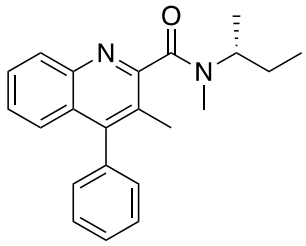

To a solution of (*R*)-(*N*-*sec*-butyl)-3-methyl-4-phenylquinoline-2-carboxamide (2.81 g, 8.82 mmol) in tetrahydrofuran (176 mL) was added sodium hydride (60% dispersion in mineral oil, 0.710 g, 17.6 mmol). The mixture was stirred at room temperature for 0.5 h, before the addition of iodomethane (2.75 mL, 44.1 mmol). The resultant solution was stirred at room temperature for 3 h and then quenched by addition of water. The aqueous phase was extracted with diethyl ether (3 × 10 mL). The combined organic phases were washed with a 10% aqueous solution of sodium thiosulfate (10 mL), brine (10 mL), dried (Na_2SO_4), filtered and concentrated *in vacuo*. Purification by flash column chromatography (petroleum ether/ethyl acetate, 3:1) gave (*R*)-(*N*-*sec*-butyl)-*N*-methyl-3-methyl-4-phenylquinoline-2-carboxamide as a white solid (2.75 g, 94%). NMR spectra showed a 1:1 mixture of rotamers. Signals for both rotamers are recorded. Mp 114–117 °C (lit.*(15)* mp 117–118 °C); IR (KBr) 2969 (CH), 1637 (CO), 1466, 1072, 731 cm^{-1}; $[\alpha]_D^{23}$ –6.3 (*c* 1.0, $CHCl_3$); ^{1}H NMR (400 MHz, $CDCl_3$) δ 0.86 (3H, t, *J* = 7.3 Hz, CH_2CH_3), 1.03 (3H, t, *J* = 7.3 Hz, CH_2CH_3), 1.24 (3H, d, *J* = 6.6 Hz, $CHCH_3$), 1.28 (3H, d, *J* = 6.6 Hz, $CHCH_3$), 1.36–1.71 (4H, m, 2 × CH_2CH_3), 2.21 (3H, s, 3-CH_3), 2.23 (3H, s, 3-CH_3), 2.73 (3H, s, NCH_3), 3.04 (3H, s, NCH_3), 3.42–3.53 (1H, m, $CHCH_3$), 4.84–4.94 (1H, m,

C*H*CH_3), 7.25–7.31 (4H, m, ArH), 7.38–7.44 (4H, m, ArH), 7.45–7.57 (6H, m, ArH), 7.60–7.67 (2H, m, ArH), 8.09 (1H, d, *J* = 8.3 Hz, ArH), 8.11 (1H, d, *J* = 8.3 Hz, ArH); ^{13}C NMR (101 MHz, $CDCl_3$) δ 11.2 (CH_3), 11.3 (CH_3), 16.0 (CH_3), 16.4 (CH_3), 17.3 (CH_3), 18.6 (CH_3), 25.5 (CH_3), 26.5 (CH_3), 27.2 (CH_2), 29.3 (CH_2), 49.6 (CH), 55.8 (CH), 124.6 (C), 125.3 (C), 125.9 (CH), 126.0 (CH), 126.7 (2 × CH), 126.8 (2 × CH), 127.4 (2 × C), 128.0 (2 × CH), 128.6 (2 × CH), 128.7 (2 × CH), 129.2 (4 × CH), 129.4 (2 × CH), 136.7 (C), 136.8 (C), 145.8 (C), 146.1 (C), 148.0 (C), 148.1 (C), 156.1 (C), 156.6 (C), 169.4 (C), 169.7 (C); MS (CI) *m/z* 333 ($M+H^+$, 100%), 291 (48), 250 (41), 220 (14), 86 (23); HRMS (CI) calcd for $C_{22}H_{25}N_2O$ ($M+H^+$), 333.1967, found 333.1972.

(*R*)-3-Bromomethyl-(*N*-*sec*-butyl)-*N*-methyl-4-phenylquinoline-2-carboxamide

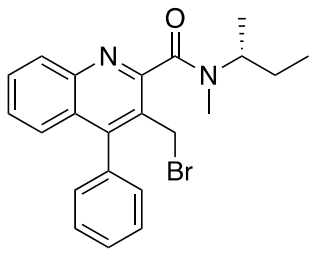

To a stirred, degassed solution of (*R*)-(*N*-*sec*-butyl)-*N*-methyl-3-methyl-4-phenylquinoline-2-carboxamide (2.70 g, 8.12 mmol) in chloroform (300 mL) was added *N*-bromosuccinimide (2.17 g, 12.2 mmol) and dibenzoyl peroxide (0.20 g, 0.812 mmol) and the solution heated under reflux for 6 h. A further portion of *N*-bromosuccinimide (1.00 g, 5.61 mmol) was then added and the solution heated under reflux for a further 16 h. The reaction mixture was cooled to room temperature, filtered and the solvent removed *in vacuo*. The crude residue was then diluted with ethyl acetate (100 mL) and washed with water (3 × 100 mL). The organic layer was dried ($MgSO_4$), filtered and concentrated *in vacuo*. Purification by flash column chromatography using a graduated eluent of

dichloromethane > dichloromethane/ethyl acetate (95:5) afforded (*R*)-3-bromomethyl-(*N*-*sec*-butyl)-*N*-methyl-4-phenylquinoline-2-carboxamide as an orange solid (2.8 g, 85%). NMR spectra showed a 2:1 mixture of rotamers. Only signals for the major rotamer are recorded. Mp 160–164 °C; IR (KBr) 2970 (CH), 1631 (CO), 1484, 1397, 1046, 766 cm^{-1}; $[\alpha]_D^{28}$ –9.0 (*c* 1.0, $CHCl_3$); ^1H NMR (400 MHz, $CDCl_3$) δ 1.09 (3H, t, *J* = 7.4 Hz, CH_2CH_3), 1.32 (3H, d, *J* = 6.8 Hz, $CHCH_3$), 1.51–1.80 (2H, m, CH_2CH_3), 2.86 (3H, s, NCH_3), 4.60 (1H, d, *J* = 10.2 Hz, 3-CHH), 4.67 (1H, d, *J* = 10.2 Hz, 3-CHH), 4.87 (1H, sextet, *J* = 6.8 Hz, $CHCH_3$), 7.37–7.48 (4H, m, ArH), 7.51–7.59 (3H, m, ArH), 7.70 (1H, ddd, *J* = 8.3, 6.7, 1.5 Hz, ArH), 8.10 (1H, dd, *J* 8.8, 8.3 Hz, ArH); ^{13}C NMR (101 MHz, $CDCl_3$) δ 11.1 (CH_3), 17.1 (CH_3), 26.6 (CH_2), 27.7 (CH_2), 30.5 (CH_3), 50.1 (CH), 126.3 (C), 126.7 (2 × CH), 127.4 (CH), 128.6 (2 × CH), 128.7 (CH), 129.0 (CH), 129.1 (CH), 129.5 (CH), 130.1 (C), 134.9 (C), 146.4 (C), 149.3 (C), 156.0 (C), 168.4 (C); MS (EI) *m/z* 410 (M^+, 5%), 298 (15), 296 (14), 217 (57), 189 (28), 151 (10), 86 (100); HRMS (EI) calcd for $C_{22}H_{23}{}^{79}BrN_2O$ (M^+), 410.0994, found 410.0992.

(*R*)-(*N*-*sec*-Butyl)-3-chloromethyl-*N*-methyl-4-phenylquinoline-2-carboxamide

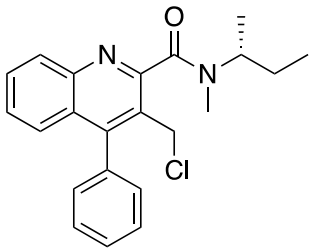

To a solution of (*R*)-3-bromomethyl-(*N*-*sec*-butyl)-*N*-methyl-4-phenylquinoline-2-carboxamide (0.500 g, 1.22 mmol) in dry tetrahydrofuran (10 mL) was added lithium chloride (0.160 g, 3.66 mmol) and the reaction mixture stirred at room temperature for 16 h. The reaction was quenched with water (30 mL) and extracted into ethyl acetate (3 ×

30 mL). The organic layers were combined and washed with brine (90 mL), dried ($MgSO_4$), filtered and concentrated *in vacuo*. The product was purified by flash column chromatography (dichloromethane/ethyl acetate, 95:5) to afford (*R*)-3-chloromethyl-(*N*-*sec*-butyl)-*N*-methyl-4-phenylquinoline-2-carboxamide as a white solid (0.331 g, 74%). NMR spectra showed a 1.5:1 mixture of rotamers. Only signals for the major rotamer are recorded. Mp 140–142 °C; IR (neat) 2970 (CH), 1620 (CO), 1481, 1404, 1219, 748 cm^{-1}; $[\alpha]_D^{24}$ –11.6 (*c* 1.0, $CHCl_3$); ^1H NMR (400 MHz, $CDCl_3$) δ 1.08 (3H, t, *J* = 7.4 Hz, CH_2CH_3), 1.30 (3H, d, *J* = 6.8 Hz, $CHCH_3$), 1.49–1.79 (2H, m, CH_2CH_3), 2.84 (3H, s, NCH_3), 4.67 (1H, d, *J* = 10.6 Hz, 3-C*H*H), 4.72 (1H, d, *J* = 10.6 Hz, 3-CH*H*), 4.82–4.92 (1H, m, $CHCH_3$), 7.36–7.61 (7H, m, ArH), 7.69–7.75 (1H, m, ArH), 8.11 (1H, dd, *J* 9.0, 8.4 Hz, ArH); ^{13}C NMR (101 MHz, $CDCl_3$) δ 11.1 (CH_3), 17.1 (CH_3), 26.6 (CH_2), 30.4 (CH_3), 40.4 (CH_2), 50.1 (CH), 125.8 (C), 126.8 (CH), 127.2 (C), 127.4 (CH), 128.5 (2 × CH), 128.7 (CH), 129.4 (CH), 129.6 (2 × CH), 130.1 (CH), 134.9 (C), 146.6 (C), 149.5 (C), 156.1 (C), 168.5 (C); MS (ESI) *m/z* 389 ($M+Na^+$, 100%); HRMS (ESI) calcd for $C_{22}H_{23}{}^{35}ClN_2NaO$ ($M+Na^+$), 389.1391, found 389.1381.

(*R*)-(*N*-*sec*-Butyl)-3-fluoromethyl-*N*-methyl-4-phenylquinoline-2-carboxamide

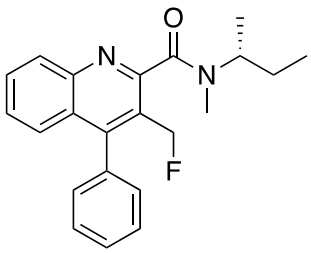

To a solution of 18-crown-6 (0.032 g, 0.12 mmol) in acetonitrile (2.5 mL) was added potassium fluoride (0.036 g, 0.61 mmol) and the resulting suspension stirred at room temperature for 0.5 h. A solution of (*R*)-3-bromomethyl-(*N*-*sec*-butyl)-*N*-methyl-4-

phenylquinoline-2-carboxamide (0.050 g, 0.12 mmol) in acetonitrile:dichloromethane (2:1, 9.0 mL) was then added dropwise and the reaction mixture heated under reflux for 72 h. Upon completion, the reaction mixture was cooled to ambient temperature and water (20 mL) was added. The solution was extracted with dichloromethane (3 × 20 mL), dried ($MgSO_4$), filtered and concentrated *in vacuo*. Purification by flash column chromatography (petroleum ether/ethyl acetate 7:3) gave (*R*)-*N*-(*sec*-butyl)-3-(fluoromethyl)-*N*-methyl-4-phenylquinoline-2-carboxamide as a white solid (0.029 g, 67%). NMR spectra showed a 3:1 mixture of rotamers. Only signals for the major rotamer are recorded. Mp 146–148 °C; IR (neat) 2972 (CH), 1628 (CO), 1559, 1485, 1398, 1049, 970 cm^{-1}; $[\alpha]_D^{30}$ –12.6 (*c* 0.5, $CHCl_3$); ^1H NMR (400 MHz, $CDCl_3$) δ 1.05 (3H, t, *J* = 7.4 Hz, CH_2CH_3), 1.29 (3H, d, *J* = 6.8 Hz, $CHCH_3$), 1.41–1.78 (2H, m, CH_2CH_3), 2.77 (3H, s, NCH_3), 4.84–4.95 (1H, m, NC*H*), 5.31 (1H, dd, *J* 20.8, 10.8 Hz, 3-C*H*H), 5.44 (1H, dd, *J* 20.8, 10.8 Hz, 3-CH*H*), 7.31–7.40 (2H, m, ArH), 7.43–7.58 (5H, m, ArH), 7.74 (1H, t, *J* 7.6 Hz, ArH), 8.17 (1H, d, *J* 8.4 Hz, ArH); ^{13}C NMR (101 MHz, $CDCl_3$) δ 10.9 (CH_3), 17.4 (CH_3), 26.5 (CH_3), 29.9 (CH_2), 50.0 (CH), 79.2 (CH_2, $^1J_{C-F}$ = 162.8 Hz), 123.0 (C, $^2J_{C-F}$ = 15.1 Hz), 127.0 (CH), 127.1 (C, $^4J_{C-F}$ = 2.3 Hz), 127.4 (CH, $^5J_{C-F}$ = 1.2 Hz), 128.5 (2 × CH), 128.7 (CH), 129.6 (2 × CH), 129.7 (CH), 130.4 (CH), 134.8 (C, $^4J_{C-F}$ = 1.5 Hz), 147.4 (C, $^3J_{C-F}$ = 2.5 Hz), 150.8 (C, $^3J_{C-F}$ = 4.7 Hz), 156.6 (C, $^5J_{C-F}$ = 2.1 Hz), 168.8 (C); MS (ESI) *m/z* 373 ($M+Na^+$, 100%); HRMS (ESI) calcd for $C_{22}H_{23}FN_2NaO$ ($M+Na^+$), 373.1687, found 373.1670. Enantiomeric excess was determined by HPLC analysis with a chiralcel AD-H column (hexane:^{i}PrOH 97.5:2.5, flow rate 1.0 mL/min), t_{major} = 30.68 and 32.22 min, t_{minor} = 27.15 and 38.38 min; er = 99.5:0.5.

In Vitro Human Competition Binding Assays

Briefly, 250 µg protein/mL in 200 µl of buffer was added to 100 µl of 1 nM ^{3}H-PK11195 (PerkinElmer, USA), together with 100 µl of test ligands PK11195 (Sigma-Aldrich, USA), PBR28 (ABX, Germany), AB5186 or LW223 at 14 different concentrations (0.001-3000 nM) for 90 min at 4 ºC. Binding was terminated with the addition of ice cold buffer before being immediately filtered over a Whatman GF/B filters (Whatman, UK) pre-treated with 0.3% polyethylenimine (Sigma-Aldrich, USA) using a Brandel harvester (Brandel, USA). Filter paper was then removed, placed into 2.5 mL of Optiphase HiSafe 3 (Perkin Elmer, USA) and counted 48 hours later on a Hidex 300 SL (Hidex, Finland). Saturation assays were performed to determine the K_d of PK11195 using a similar protocol, except that 6 concentrations of ^{3}H-PK11195 (1.6-200 nM) were used alongside 10 µM of PK11195 to determine non-specific binding. All binding assays were performed in triplicate.

GraphPad Prism version 6 (GraphPad Software, USA) was used to fit all binding affinity curves. A comparison of a one-site and two-site models was made using the least squares algorithm and model selection was compared using an F test. The null hypothesis (one-site fitting as more suitable) was rejected if $p<0.05$. Normalized mean %SB of each group (HAB, MAB or LAB) and a K_d value of 14.0nM (determined based on saturation binding results, Sup.Fig.2) was used to determine the best fitting model and to calculate LAB:HAB ratios. Affinity values (K_i) were calculated by fitting individual tissue samples again with a K_d 14.0nM.

Invasive Input Function Measurement

Polyethylene catheters (PE50) filled with heparinized saline (20 IU/mL) were inserted into the left femoral artery and vein with the help of a stereomicroscope and securely fastened with ligatures (6-0 silk thread). Catheters were held in place with surgical glue.

Rat Myocardial Infarction Procedure

Briefly, the skin was incised at the level of the left third and fourth ribs where the pectoral muscles were divided and retracted. Left lateral thoracotomy was then performed. With minimal handling, the pericardium was ruptured and the heart gently exteriorized from the thorax, and a nonabsorbable 5-0 ligature was placed around the left anterior descending coronary artery just above the bifurcation of the first diagonal and maneuvered back into position. Before wound closure, a drain was inserted to assist with removal of air and fluid from the thorax. Once removed, the wound was then closed in three layers. Animals were recovered and extubated once spontaneous ventilation was established, housed at 30 °C for 24 hours and given sterile sodium chloride 0.9% 0.01 mL/g fluid therapy subcutaneously in addition to another dose of Buprenorphine. After 24 hours, normal housing conditions were resumed.

Radiometabolite Blood and Tissue Processing and Analysis

All blood samples were 1 mL each and manually collected from different animals to generate a population curve, in order to respect total blood volume limits for terminal arterial blood collections in rats. Following blood and tissue collection, all samples were

kept on ice until analyzed. Radioactivity in whole blood and plasma, as well as homogenized tissue samples, was assessed using a well-type γ-counter using a 400–1400 keV window (Perkin Elmer Wizzard2, USA). Plasma samples (400 µl) and tissue samples (500 µl) were processed by acetonitrile denaturation (1:1.4 v/v) and analyzed by HPLC (Ultimate2000, ThermoFisher, UK) on a Luna C18(2) 10×250 mm, 10 µm column (Phenomenex, UK) with acetonitrile/water 70/30 and flow rate of 4 mL/min to estimate the parent fraction. The plasma f_p was determined using ultrafiltration units (Centrifree® 30K, Millipore, UK).

Simulation of Changes in ^{18}F-LW223 BP_{ND} for varying blood flow scenarios

Simulation work was carried out using a Matlab (MathWorks, USA) 2-tissue compartment code with Ordinary Differential Equation (ODE) solvers. Six different levels of K_1 values (0.9, 0.7, 0.5, 0.3, 0.1 and 0.01 mL/min/cc) were tested with fixed k_2 and vB=0.05. The following BP_{ND} values were simulated: 4, 10, 16 and 20; with k_3 modified and k_4 fixed. All micro parameters used in the simulations are shown in Supplemental Table 5. The input function used was an average of the blood curves taken from healthy animals using the SwissTrace blood sampler (Supplemental Data File 1). The plasma to whole blood ratio used was 1.84 and the AIF was metabolite corrected using a population based curve as in the experimental data. All modelled time-activity curves were noise free. Outcome measures were estimated using Turku code (fitk4, http://www.turkupetcentre.net/petanalysis/tpcclib/doc/fitk4.html) and operational equations for 2-tissue curve fitting. The minimisation code used Topographical Global Optimisation based on an algorithm by Aimo Torn and Sami Viitanen

(www.abo.fi/~atorn/ProbAlg/Page53.html). Calculated BP_{ND} for each simulated scenario was compared with truth BP_{ND}. All parameters estimated with the parameter standard deviation for K_1 and BP_{ND} are reported in Supplemental Table 6.

Ex Vivo Immunofluorescence Imaging

Briefly, antigen retrieval was carried out in a pressure cooker using tris-EDTA (pH 9) before an endogenous peroxidase block (3% H_2O_2, 15 min) and tissue permeabilization/ blocking in 10% donkey serum (PBS, 0.1% Triton X-100) for 1 hour room at temperature. The CD68 primary antibody (1/100 in 1% donkey serum, MCA341R, Bio-Rad, USA) was incubated with the slides overnight at 4 °C, followed by incubation with the first secondary antibody (1/750 in 1% donkey serum, donkey anti-mouse-HRP, 715-036-150, Jackson ImmunoResearch, USA) for 1 hour at room temperature. This first secondary antibody was visualized using the TSA system (Cyanine 3 System, 1/50 for 4 min, Perkin Elmer, UK). Microwave antigen retrieval (tris-EDTA pH 9) was then carried out to destroy the CD68-associated antibodies, leaving behind the visualization product only. An additional endogenous peroxidase and serum block was performed before incubation with the TSPO primary antibody (1/100 in 1% donkey serum, ab109497, Abcam, UK) for 1 hour at room temperature. A subsequent secondary antibody incubation was performed at 1 hour room temperature (1/750 in 1% donkey serum, donkey anti-rabbit-HRP, 711-036-152, Jackson ImmunoResearch, USA) before visualization with the TSA reagent (Cyanine 5 System, 1/50 for 4 min, Perkin Elmer, UK). The slides were then counterstained with DAPI and mounted.

Autoradiography

Rehydrated tissue on glass slides was incubated in assay buffer (50 mM Tris Buffer) for 30 min prior to the experiment. The slides were then incubated with ^{18}F-LW223 (50 nM in assay buffer) for 1 hour at room temperature. Slides were washed twice in assay buffer followed by a dip in $_{d}H_2O$. The slides were then dried and exposed to an autoradiography plate (BAS-IP-SR 2040 super resolution screen, Cytiva, USA) and imaged on an autoradiography imager (Amersham Typhoon IP Biomolecular Imager, Cytiva, USA). Images were analyzed using Image J, using the ratio of signal within a ROI to the background signal on each slide to calculate the tissue to background ratio (TBR).

SUPPLEMENTARY RESULTS

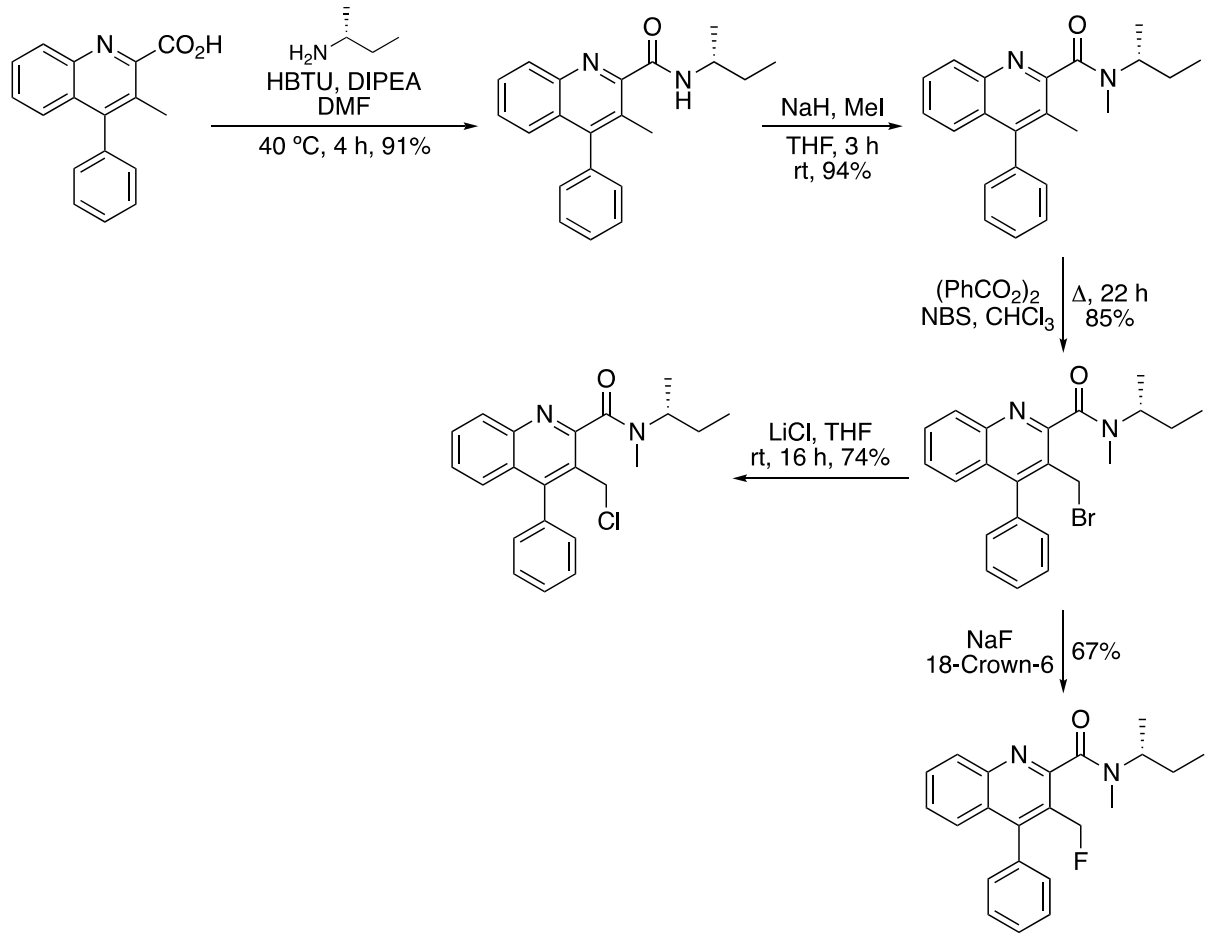

Supplemental Figure. 1. Four step synthesis of chloride precursor and LW223 from 3-methyl-4-phenylquinoline-2-carboxylic acid.

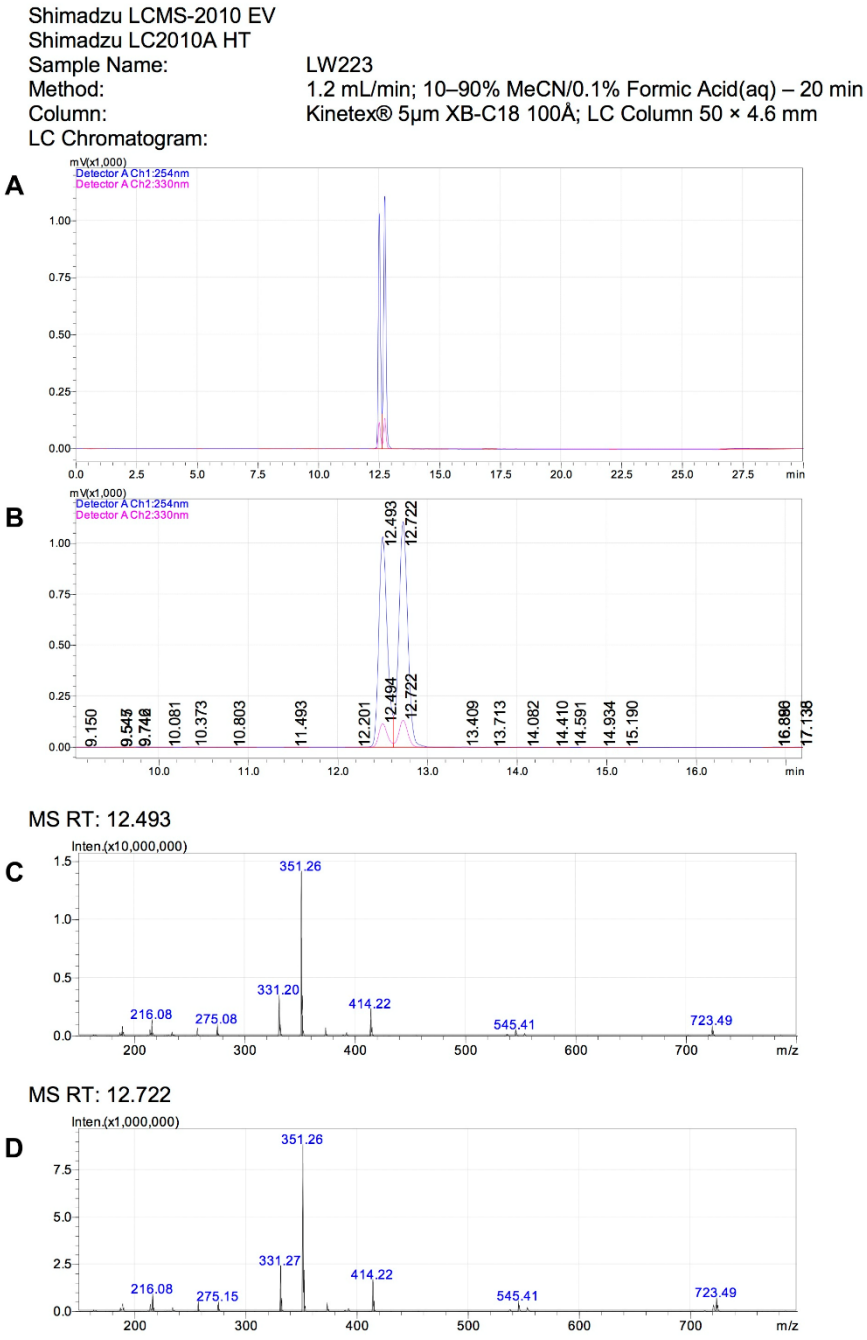

Supplemental Figure 2. HPLC and MS analysis of LW223 rotamers. A) LCMS trace of LW223 showing existence of two rotamers. **B)** Expansion of LC-MS trace of LW223. **C)** MS of first rotamer (12.493 minutes). **D)** MS of second rotamer (12.722 minutes).

Brain Tissue for Binding Assays	Heart Tissue for Binding Assays
25055	7626
24781	26124
24778	20592
22629	25055
21396	001.29466
18391	2580
9508	26309
4176	29084
13410	3784
2564	4176
3785	18393
3783	3786
2576	18392
2575	25751
2572	22611
2562	9508
2559	2473
2558	
2552	
2551	
2550	
2452	
24340	
22630	
22628	
22612	
20593	
20121	
18407	
15809	

Supplemental Table 1. Edinburgh Brain and Tissue Bank BNN reference number for all tissues utilized from the bank.

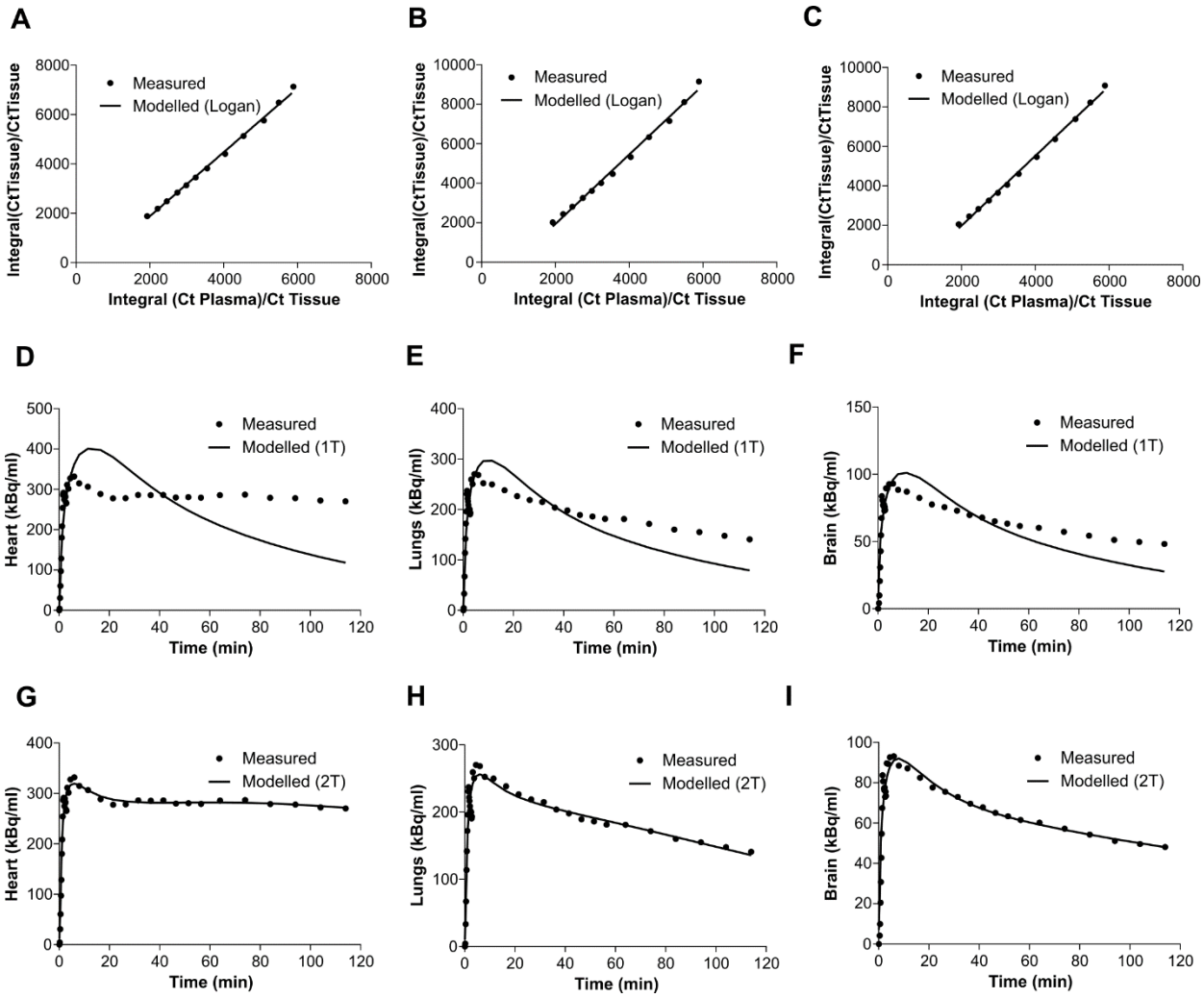

Supplemental Figure 3. Representative examples of different models versus measured data on naive rat organs. A) Logan modelling in the heart, **B)** lung and **C)** brain. Modelling constrained to a t^*=30min. **D)** 1T modelling in the heart, **E)** lung and **F)** brain. **G)** 2T modelling in the heart, **H)** lung and **I)** brain.

Region	Group	AIC (Mean± SEM)		
		2T	1T	Logan
Heart	Naive	47.8± 6.3	131.9± 2.7	125.8± 4.4
	MI	52.1± 4.2	135.5± 4.8	132.7± 1.6
	Blocked Naive	132± 27.3	110.2± 31.5	118.1± 6.3
LV Anterior Wall	Naive	127.9± 12.4	159.1± 6.2	144.5± 1.9
	MI	121.5± 8.9	143.7± 7.1	151.7± 2.1
	Blocked Naive	160.7± 15.5	136.6± 3.9	148.6± 5.1
Brain	Naive	42.8± 3.4	100.6± 4.8	117.1± 3.1
	MI	57.8± 12.9	118.8± 9.7	118.6± 3.5
	Blocked Naive	153.3± 18	128.9± 4.4	128.3± 5.3
Lungs	Naive	62.6± 5.7	105.4± 4.1	112.6± 2.8
	MI	60.7± 4	123.9± 7.8	120.7± 2.6
	Blocked Naive	156.5± 21.4	138.1± 1.8	119.6± 6.5
	Group Mean	98.0	127.8	128.2

Supplemental Table 2. The Akaike information criterion (AIC) for assessed models in all animals and regions used in this study, naive *n* = 6, MI *n* = 9, blocked naive *n* = 3.

Organ	Mouse % Total body weight	Human % Total body weight	Correction Factor
Brain	1.62	1.93	1.19
Heart	0.48	0.43	0.89
Lung	0.53	1.36	2.55
Gall Bladder	0.03	0.01	0.44
Liver	4.00	2.59	0.65
Gut	5.01	0.92	0.18
Adrenals	0.02	0.02	1.09
Kidney	1.28	0.41	0.32
Bladder	0.08	0.06	0.76

Supplemental Table 3. Scaling factors for different organs in mice and humans based on their percentage contribution to total body weight. Data presented in this table was calculated based on previously published data.

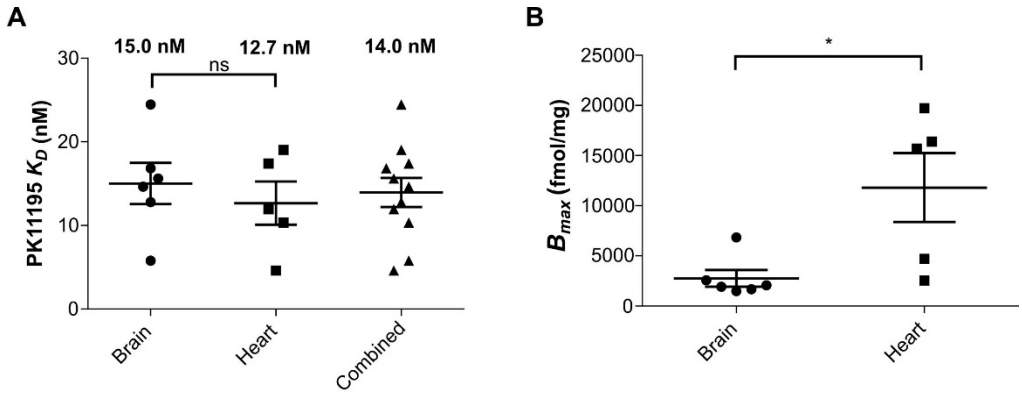

Supplemental Figure 4. Dissociation constant (K_d) values and maximal binding (B_{max}) of PK11195 in human brain and heart. A) K_d values of PK11195 and **B)** B_{max} calculated from saturation binding assays. Results represent the mean±S.E.M., brain n = 6, heart n = 5, ns=not significant, *=p<0.05 using an unpaired t-test for brain versus heart.

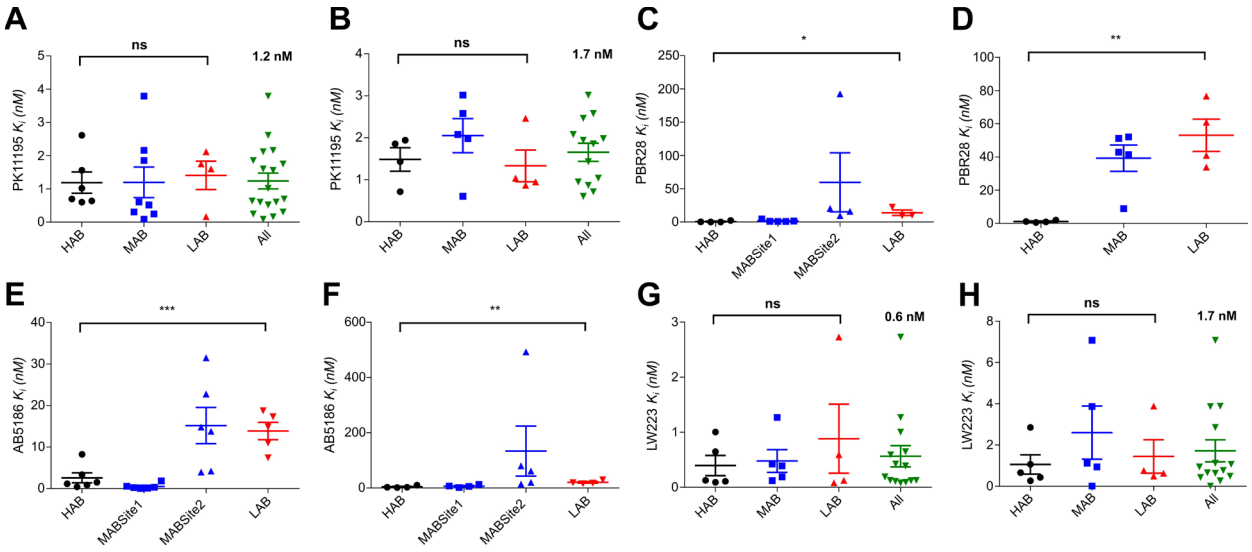

Supplemental Figure 5. Individually calculated K_i values for TSPO ligands using human brain and heart. A) PK11195 binding affinities in brain calculated using one-site fitting, HAB *n* = 6, MAB *n* = 8 and LAB *n* = 4 and **B)** heart calculated using a one-site fitting, HAB *n* = 4, MAB *n* = 5 and LAB *n* = 4. **C)** PBR28 binding affinities in brain calculated using a one-site fitting apart from MAB where a two-site fitting was used, HAB *n* = 4, MAB *n* = 5 and LAB *n* = 4 and **D)** heart calculated using a one-site fitting, HAB *n* = 4, MAB *n* = 5 and LAB *n* = 4. **E)** AB5186 binding affinities in brain calculated using a one-site fitting apart from MAB where a two-site fitting was used, HAB *n* = 6, MAB *n* = 6 and LAB *n* = 5 and **F)** heart using a one-site fitting apart from MAB where a two-site fitting was used, HAB *n* = 4, MAB *n* = 5 and LAB *n* = 4. **G)** LW223 binding affinities in brain calculated using a one-site fitting, HAB *n* = 5, MAB *n* = 5 and LAB *n* = 4 and **H)** heart calculated using a one-site fitting, HAB *n* = 5, MAB *n* = 5 and LAB *n* = 4. ns=not significant, *=p<0.05, **=p≤0.01 and ***=p≤0.001 using an unpaired *t*-test for HAB vs. LAB. All results represent the mean±SEM.

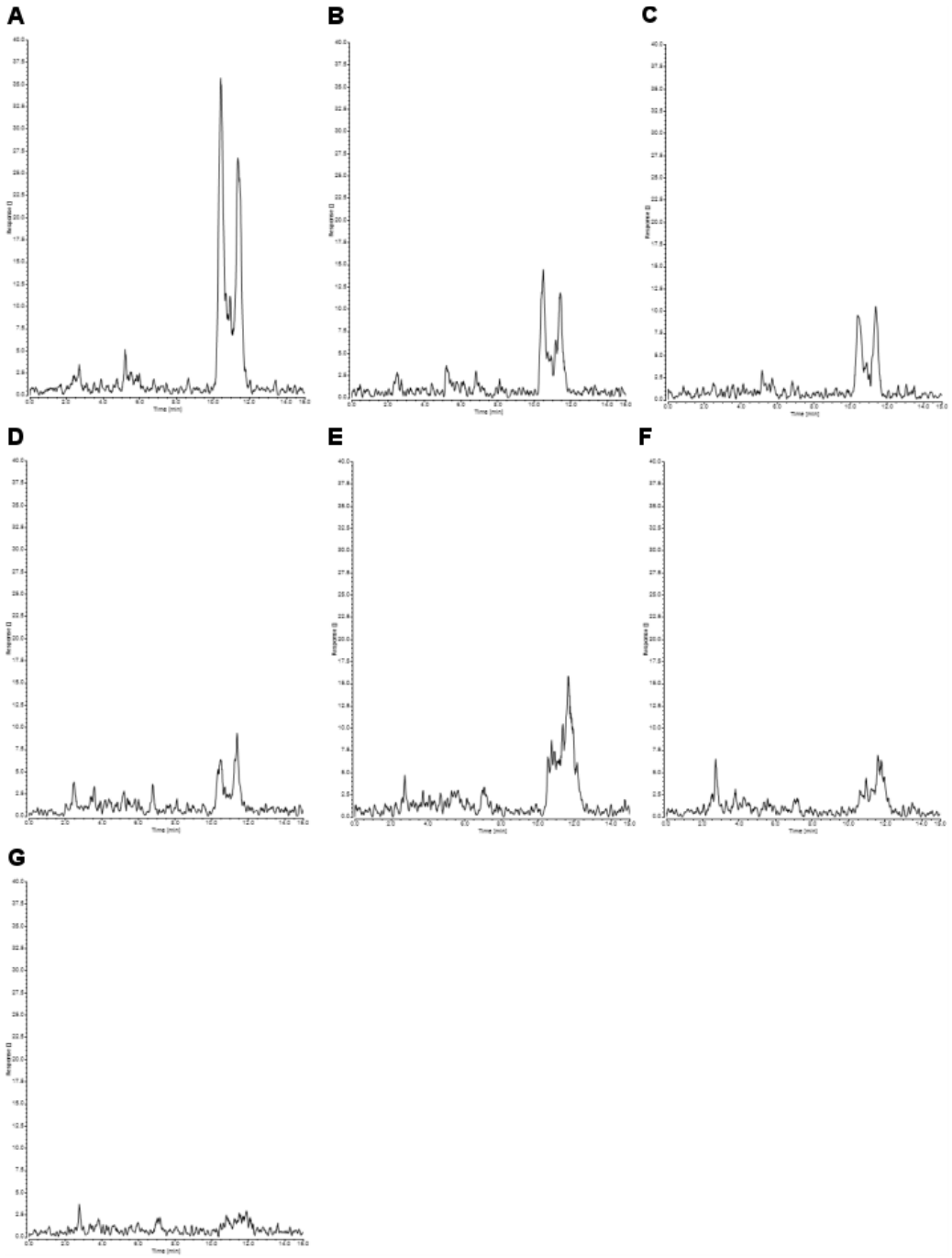

Supplemental Figure 6. Representative chromatograms of arterial blood sampled at 2-120 min post-injection of ^{18}F-LW223. A) Radiodetection of parent peak and radiometabolites in rat atrial plasma at 2 min, **B)** 5 min, **C)** 10 min, **D)** 20 min, **E)** 30 min, **F)** 60 min and **G)** 120 min post intravenous bolus administration of ^{18}F-LW223.

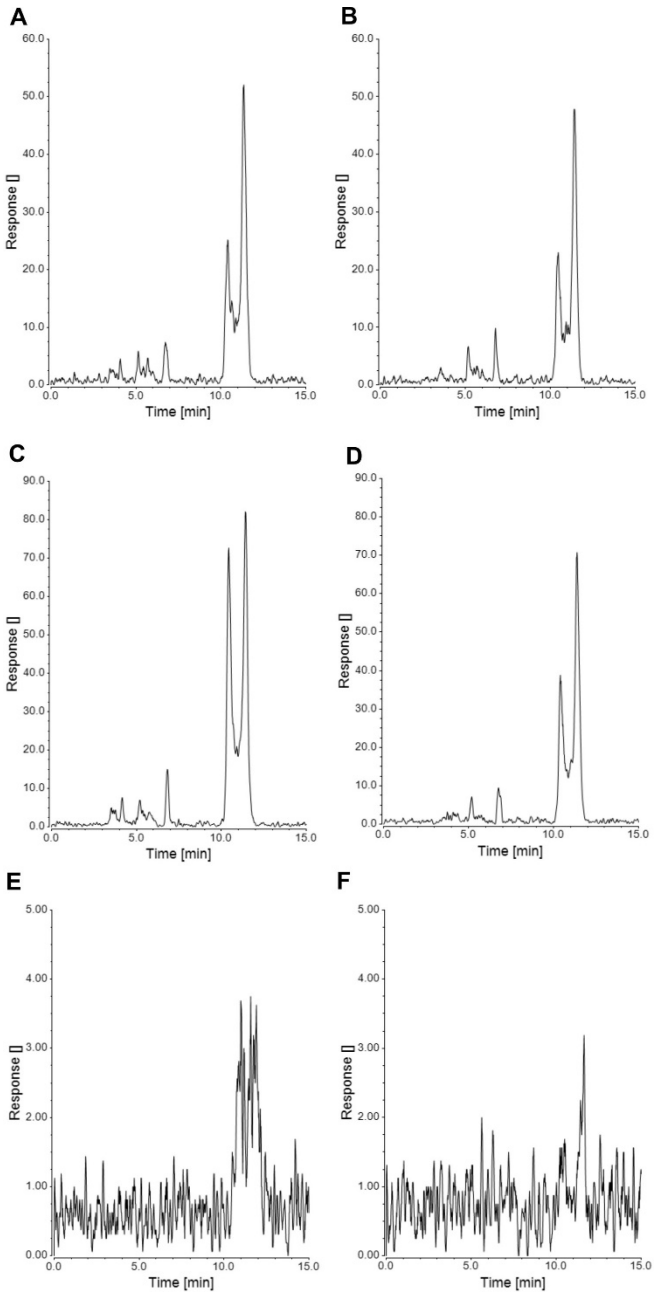

Supplemental Figure 7. Representative chromatograms of organs sampled at 60 and 120 min post-injection of ^{18}F-LW223. A) Radiodetection of parent peak and radiometabolites in rat heart at 60 min, **B)** heart at 120 min post injection, **C)** lung at 60 min, **D)** lung at 120 min, **E)** brain at 60 min and **F)** brain at 120 min post intravenous bolus administration of ^{18}F-LW223.

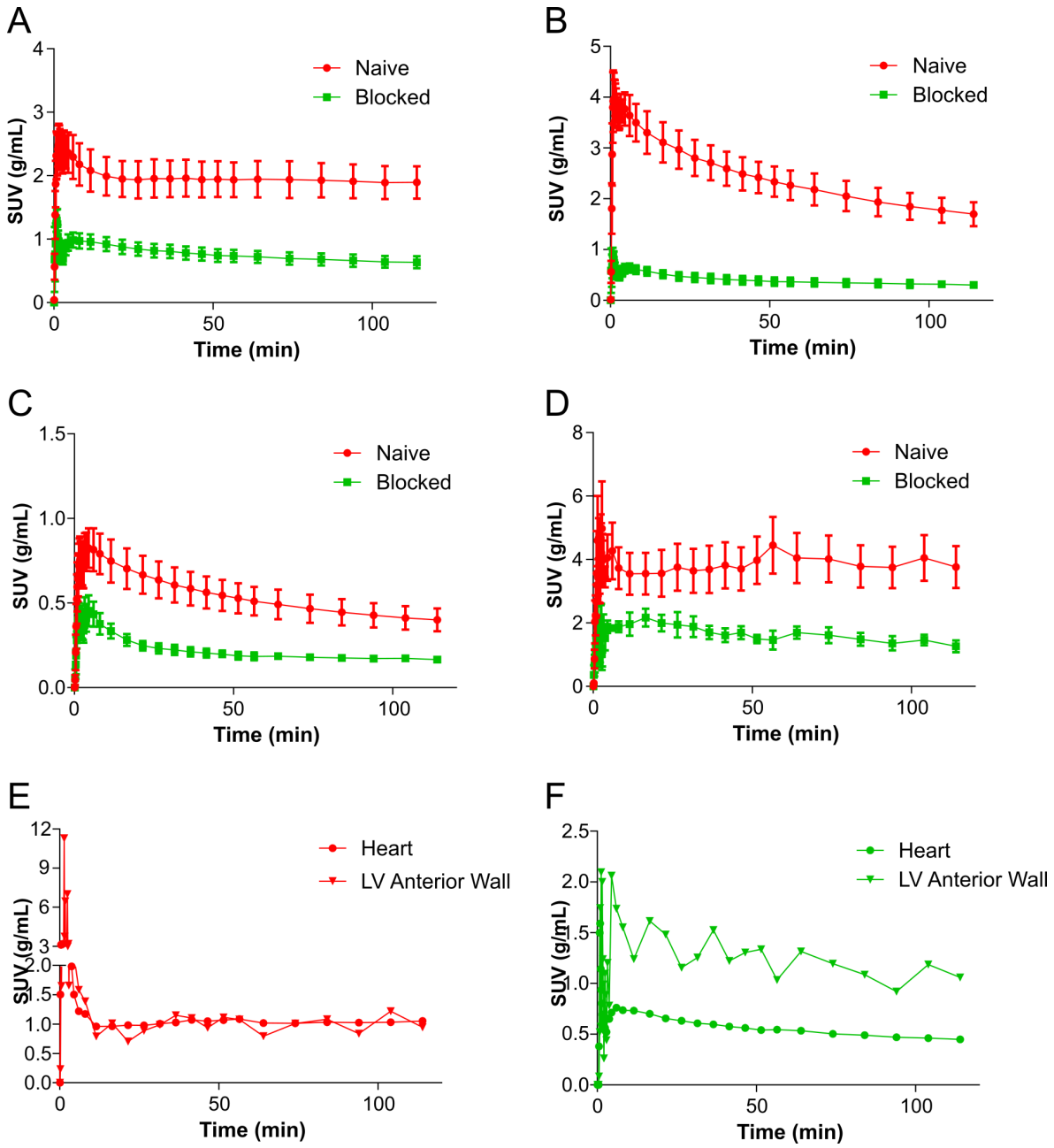

Supplemental Figure 8. SUV time activity curves in naive and naive blocking studies. A) The effect of PK11195 blockade (1 mg/kg) on ^{18}F-LW223 in the heart, **B)** lung, **C)** brain and **D)** sampled left ventricle (LV) anterior wall. Mean ±SEM, naive *n* = 6, blocked *n* = 3. **E)** Example time activity curves from a single naive and **F)** blocked naive animal demonstrating the noise which is present in the LV subregion sample.

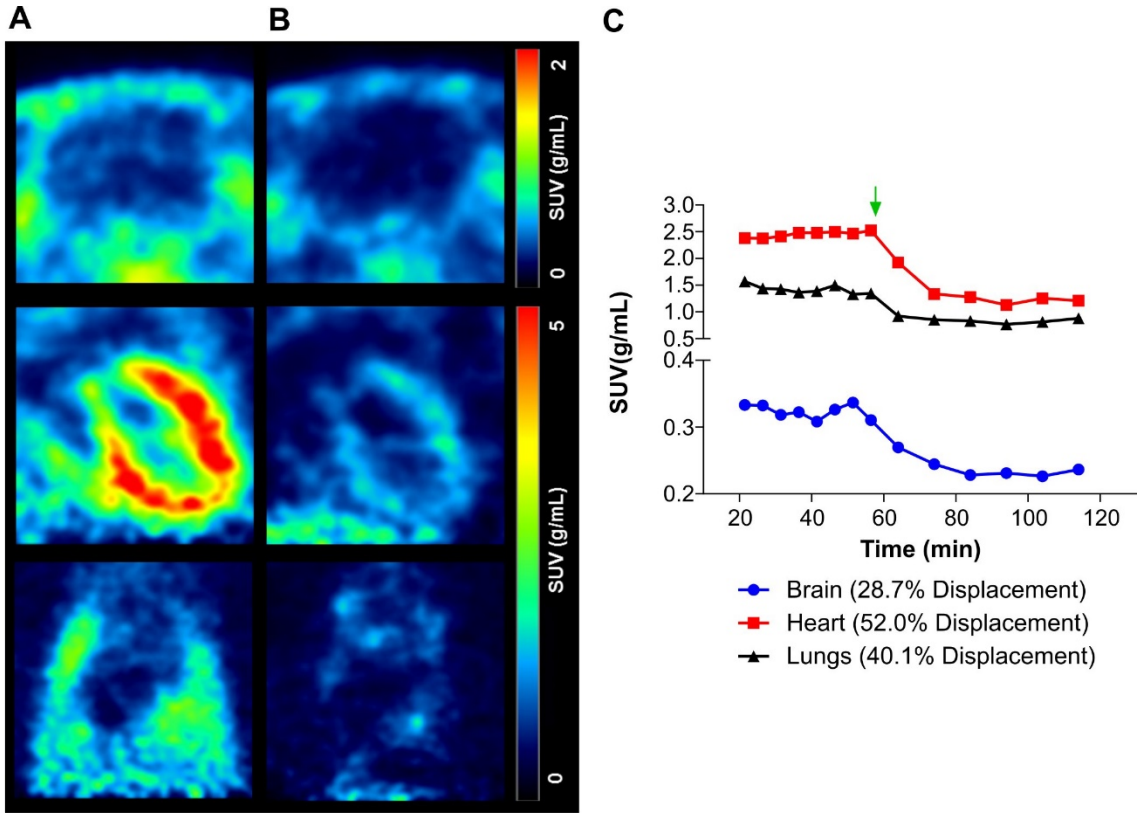

Supplemental Figure 9. ***In vivo*** **displacement of ^{18}F-LW223 using PK11195 in naive rats. A)** SUV sum image of ^{18}F-LW223 uptake before and after **B)** displacement with PK11195 (1mg/kg). Top row=brain, middle row=heart and bottom row=lung. Baseline images are averaged before (45-60 min) and displacement images are averaged after (95-120 min) PK11195 administration. **C)** Time activity curve of ^{18}F-LW223 before and after (green arrow) PK11195 challenge.

Region	Group	K1		k2		k3		k4		k3/k4		VT	
		Mean± S.E.M.	% SE± S.E.M	Mean± S.E.M.	% SE± S.E.M	Mean± S.E.M.	% SE± S.E.M	Mean± S.E.M.	% SE± S.E.M	Mean± S.E.M.	% SE± S.E.M	Mean± S.E.M.	% SE± S.E.M
Global Heart	Naive	0.58± 0.06	6.09± 0.99	0.33± 0.01	12.24± 1.51	0.031± 0.004	18.51± 2.04	0.01± 0.00	46.319± 9.764	4.77± 0.27	32.43± 7.72	9.93± 0.98	29.09± 6.83
	MI	0.58± 0.04	6.57± 0.71	0.36± 0.03	13.46± 1.07	0.04± 0.004	17.38± 1.46	0.01± 0.00	38.834± 5.141	6.62± 0.98	26.94± 4.09	12.57± 1.39	25.22± 4.06
	Blocked Naive	0.19± 0.01	68.38± 50.01	0.23± 0.02	464.35± 402.47	0.721± 0.638	66.85± 24.71	0.13± 0.11	475.458± 399.637	4.52± 0.66	472.01± 411.64	4.56± 0.22	23.00± 13.02
LV Anterior Wall	Naive	0.9± 0.11	15.67± 1.03	0.26± 0.03	36.50± 3.72	0.033± 0.005	59.73± 13.92	0.00± 0.00	224.581± 74.786	7.99± 1.21	176.71± 61.63	29.95± 3	164.47± 53.64
	MI	0.25± 0.03	13.95± 1.42	0.18± 0.02	36.24± 3.63	0.025± 0.003	71.52± 12.28	0.01± 0.00	267.21± 58.427	7.92± 1.31	216.05± 57.91	13.62± 3.21	201.04± 55.93
	Blocked Naive	0.28± 0.01	115.97± 106.93	0.08± 0.03	1463.29± 1425.50	0.855± 0.854	542.66± 354.24	0.23± 0.23	105717.505± 102167.414	12.64± 8.90	105197.46± 101812.77	75.25± 63.13	98934.28± 98923.61
Brain	Naive	0.14± 0.02	3.82± 0.21	0.18± 0.02	9.89± 0.58	0.016± 0.001	31.48± 2.63	0.01± 0.00	41.74± 3.31	1.22± 0.10	20.4± 2.51	1.6± 0.17	12.69± 2.08
	MI	0.17± 0.01	5.12± 0.69	0.19± 0.01	13.53± 1.84	0.023± 0.003	36.80± 6.29	0.02± 0.00	50.061± 13.8	1.42± 0.08	26.99± 7.8	2.21± 0.24	17.20± 5.84
	Blocked Naive	0.06± 0	471.22± 154.47	0.11± 0.02	18048.79± 12808.17	2.324± 1.818	15742.04± 3854.98	2.33± 1.03	20944.155± 15962.239	0.71± 0.32	36685.81± 19130.43	0.93± 0.02	21.85± 4.74
Lung	Naive	0.94± 0.06	6.51± 0.78	0.32± 0.02	13.99± 1.06	0.031± 0.007	32.87± 3.51	0.02± 0.00	38.458± 7.495	1.38± 0.13	20.15± 2.97	6.94± 0.51	10.89± 2.35
	MI	1.08± 0.17	7.24± 0.8	0.39± 0.07	15.09± 1.01	0.046± 0.011	24.35± 2.09	0.02± 0.00	26.524± 3	2.49± 0.34	15.17± 1.02	10.43± 1.60	9.36± 0.93
	Blocked Naive	0.16± 0.04	19± 5.43	0.35± 0.16	82.05± 23.02	0.181± 0.119	132.22± 30.37	0.05± 0.03	102.311± 49.984	3.19± 0.41	98.05± 26.56	2.2± 0.19	37.68± 22.85

Supplemental Table 4. Kinetic modelling data for 2T analysis of ^{18}F-LW223 uptake in naive, myocardial infarction (MI) and blocked rats (post injection of PK11195, 1mg/kg). Naive *n* = 6, MI *n* = 5, Blocked *n* = 3.

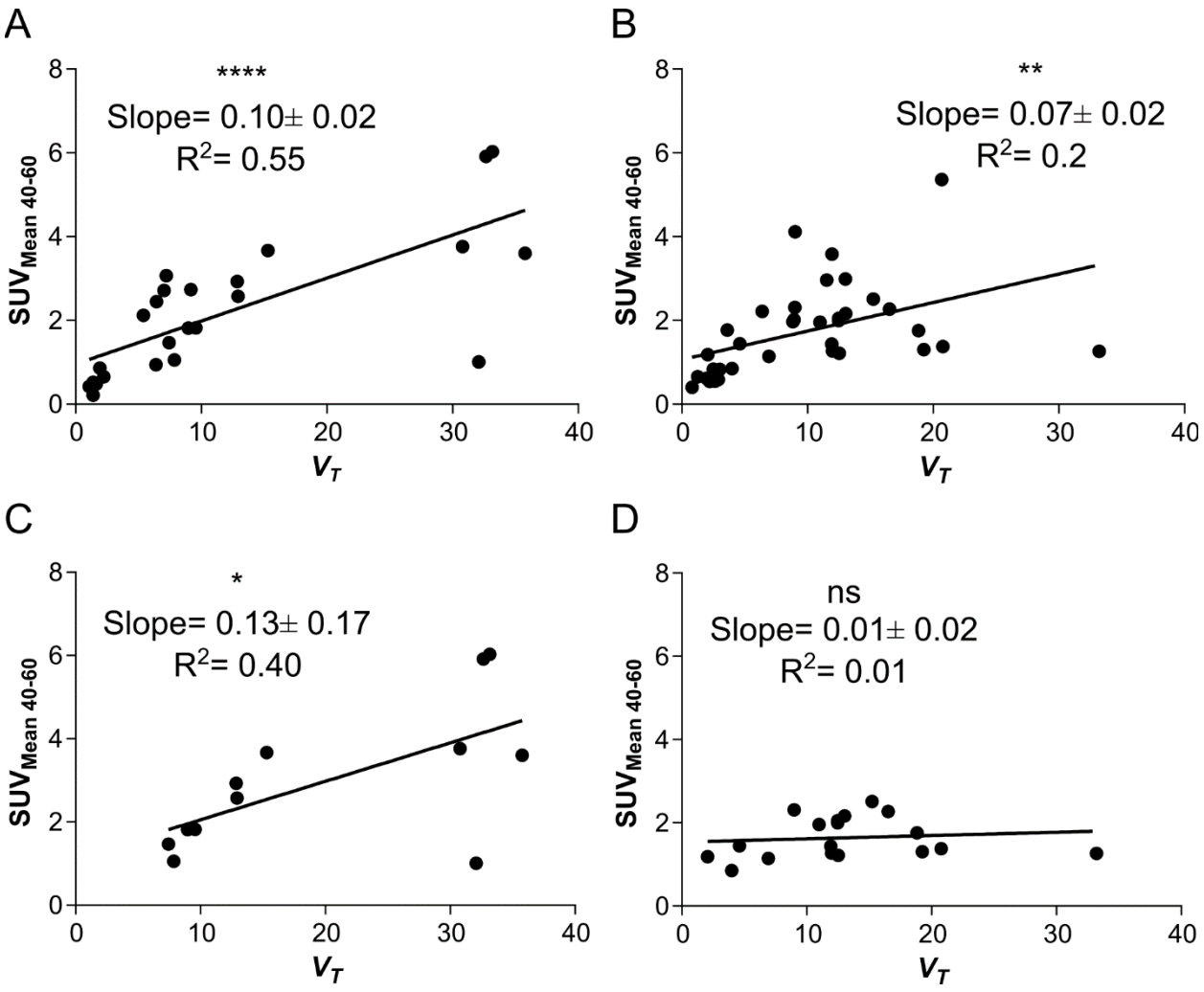

Supplemental Figure 10. Correlation of V_T and SUV in naive and MI animals. A) Global heart, left ventricle sample, brain and lung correlation in naive rats and **B)** MI rats. **C)** Global heart and left ventricle sample correlation in naive rats and **D)** MI rats. Naive *n* = 6, MI *n* = 9, *=p<0.05, **=p<0.01 and ****=p<0.0001 using Pearson correlation.

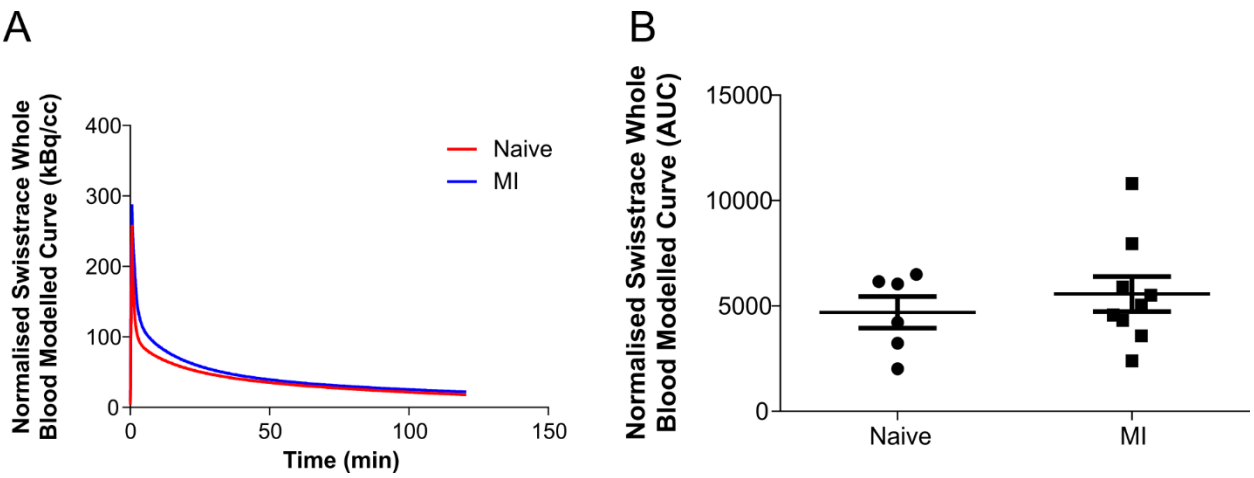

Supplemental Figure 11. Invasive input function measurements in naive and MI rats during ^{18}F-LW223 PET. A) Average time activity curve of whole blood modelled and normalized to injection dose. **B)** Area under the curve for each individual blood curve normalized to injection dose. Naive *n* = 6, MI *n* = 9, mean ±SEM.

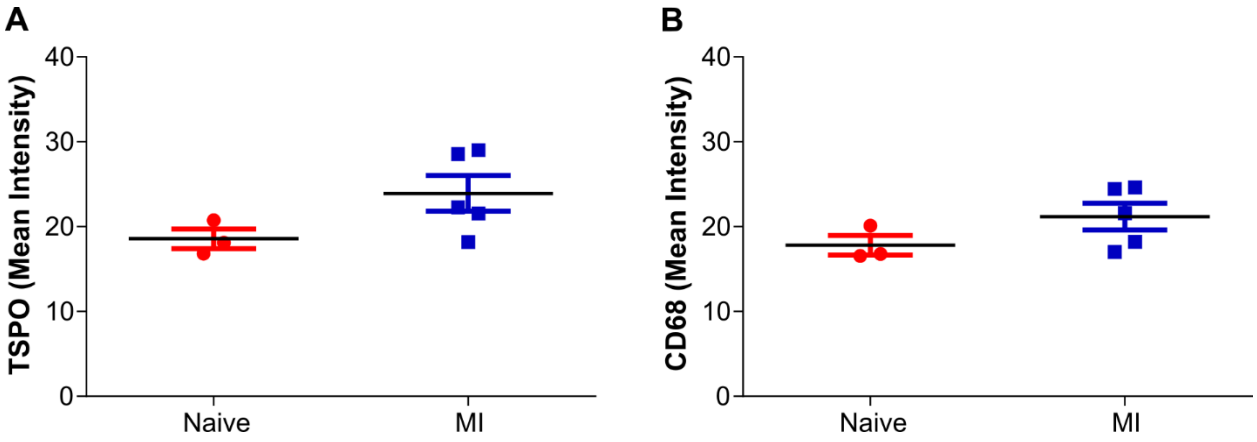

Supplemental Figure 12. *Ex-vivo* immunofluorescent staining within the posterior left ventricle. A) TSPO expression sampled within the posterior wall of the left ventricle in naive and MI hearts. **B)** CD68 expression sampled within the posterior wall of the left ventricle in naive and MI hearts. Results represent the mean±S.E.M., naive *n* = 3, MI *n* = 5.

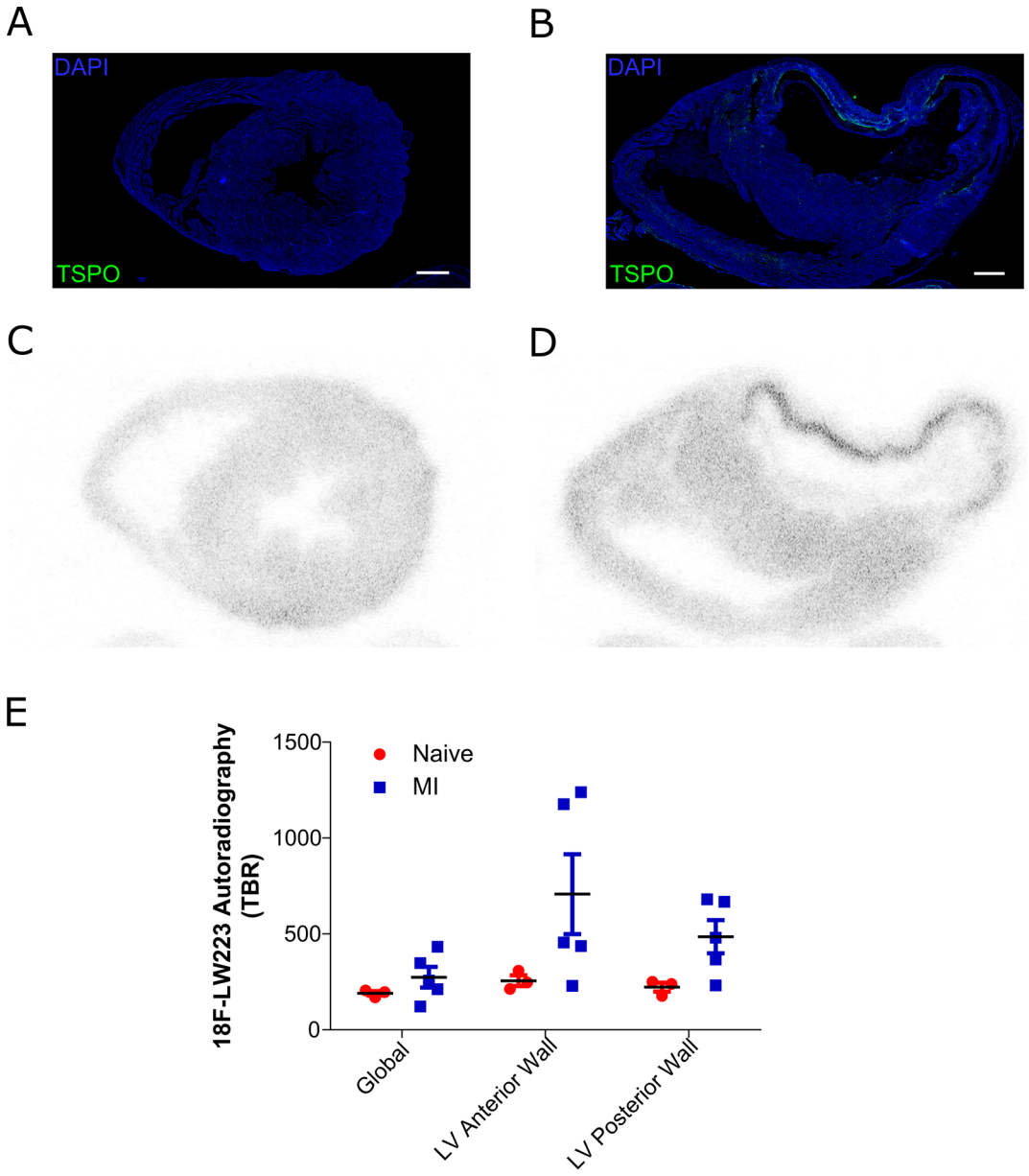

Supplemental Figure 13. ^{18}F-LW223 Autoradiography. A) Example TSPO immunofluorescent staining in naive and **B)** MI hearts. **C)** Example autoradiography image of the same naive and **D**) MI heart. **E)** Quantification of the autoradiography in the global heart and left ventricle (LV) anterior wall. Results represent the mean±S.E.M., naive n = 3, MI n = 5.

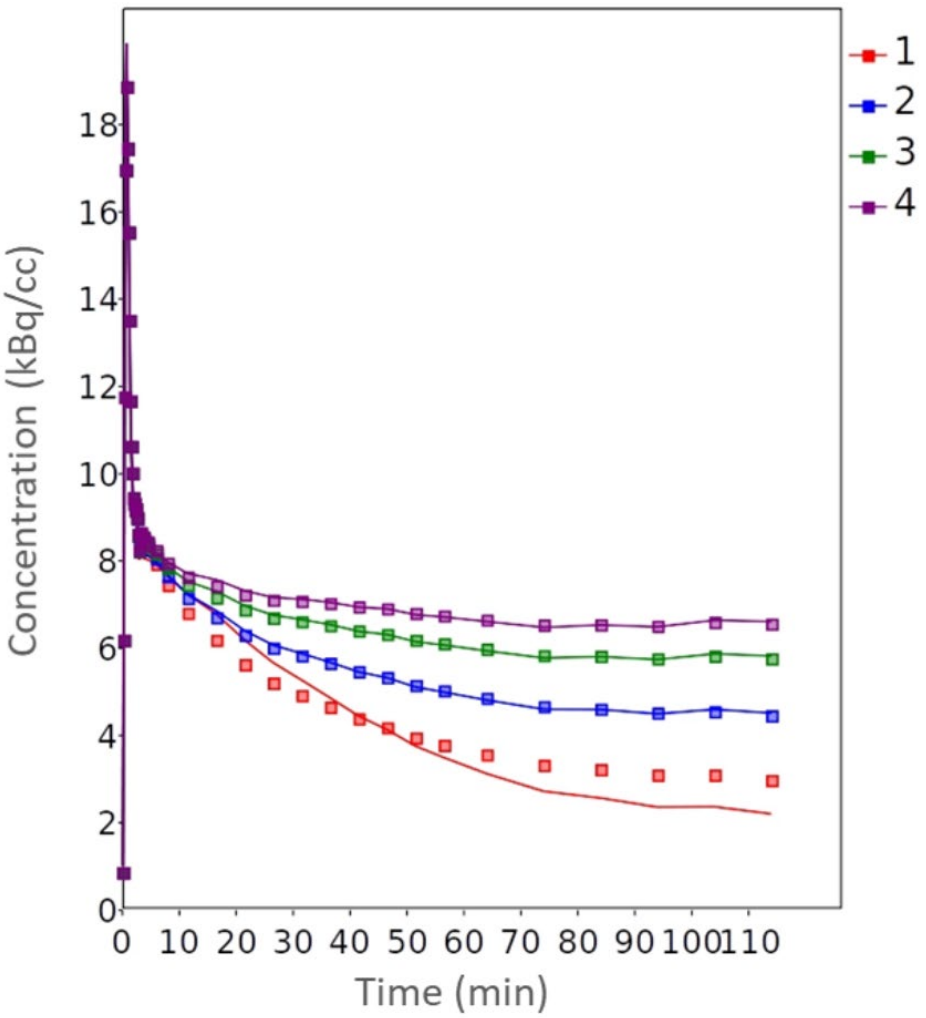

Supplemental Figure 14. Simulation on the effect of changes in K_1 on BP_{ND}. Example of simulated curves with lowest K_1=0.01 mL/mim/cc and 4 different BP_{ND} values (1= BP_{ND} of 4; 2= BP_{ND} of 10; 3= BP_{ND} of 16; and 4= BP_{ND} of 20). All simulated curves are noise free.

Curve	K_1 simulated	k_2 simulated	k_3 simulated	k_4 simulated	BP_{ND} simulated
1	0.9	0.3	0.02	0.005	4
2	0.9	0.3	0.05	0.005	10
3	0.9	0.3	0.08	0.005	16
4	0.9	0.3	0.1	0.005	20
5	0.7	0.3	0.02	0.005	4
6	0.7	0.3	0.05	0.005	10
7	0.7	0.3	0.08	0.005	16
8	0.7	0.3	0.1	0.005	20
9	0.5	0.3	0.02	0.005	4
10	0.5	0.3	0.05	0.005	10
11	0.5	0.3	0.08	0.005	16
12	0.5	0.3	0.1	0.005	20
13	0.3	0.3	0.02	0.005	4
14	0.3	0.3	0.05	0.005	10
15	0.3	0.3	0.08	0.005	16
16	0.3	0.3	0.1	0.005	20
17	0.1	0.3	0.02	0.005	4
18	0.1	0.3	0.05	0.005	10
19	0.1	0.3	0.08	0.005	16
20	0.1	0.3	0.1	0.005	20
21	0.01	0.3	0.02	0.005	4
22	0.01	0.3	0.05	0.005	10
23	0.01	0.3	0.08	0.005	16
24	0.01	0.3	0.1	0.005	20

Supplemental Table 5. Kinetic parameters used in simulations. The blood volume (vB) was kept at 5% or 0.05 for all simulations. These parameters were based on the results of the modelling presented in the paper.

urve	K_1 estimated	K_1 %SD	k_2 estimated	k_3 estimated	k_4 estimated	BP_{ND} estimated	BP_{ND} %SD	BP_{ND} simulated – BP_{ND} estimated	BP_{ND} % difference	BP_{TC} estimated	Weighted sum of squares	2TCM AIC
1	0.844	0.367	0.276	0.019	0.005	4.106	4.689	-0.106	-2.648	4.865	58.295	24.853
2	0.841	0.416	0.271	0.048	0.005	9.839	2.044	0.161	1.611	11.703	55.936	23.242
3	0.838	0.442	0.266	0.077	0.005	15.422	1.366	0.578	3.613	18.410	55.344	22.827
4	0.836	0.455	0.263	0.096	0.005	19.004	1.185	0.996	4.980	22.737	55.372	22.847
5	0.656	0.396	0.275	0.019	0.005	4.127	4.397	-0.127	-3.183	6.289	36.972	7.094
6	0.654	0.428	0.270	0.048	0.005	9.844	1.931	0.156	1.560	15.061	35.091	5.058
7	0.651	0.415	0.265	0.077	0.005	15.374	1.413	0.626	3.913	23.612	34.263	4.126
8	0.650	0.462	0.262	0.096	0.005	18.957	1.212	1.043	5.215	29.187	34.019	3.848
9	0.467	0.429	0.274	0.019	0.005	4.131	5.080	-0.131	-3.270	8.851	20.523	-15.860
10	0.465	0.387	0.269	0.048	0.005	9.832	1.802	0.168	1.680	21.153	19.270	-18.320
11	0.463	0.497	0.263	0.077	0.005	15.347	1.490	0.653	4.081	33.154	18.721	-19.450
12	0.462	0.282	0.260	0.096	0.005	18.900	1.313	1.100	5.500	40.936	18.504	-19.900
13	0.279	0.467	0.271	0.019	0.005	4.163	6.155	-0.163	-4.062	14.946	9.359	-46.490
14	0.277	0.469	0.266	0.048	0.005	9.824	2.093	0.176	1.758	35.441	8.706	-49.310
15	0.276	0.507	0.260	0.076	0.005	15.284	1.480	0.716	4.475	55.397	8.418	-50.620
16	0.275	0.472	0.256	0.095	0.005	18.802	1.310	1.198	5.990	68.321	8.280	-51.260
17	0.090	0.664	0.260	0.018	0.004	4.354	12.591	-0.354	-8.838	48.158	3.830	-81.330
18	0.090	0.891	0.252	0.046	0.005	9.818	4.715	0.182	1.824	109.327	3.573	-84.040
19	0.089	0.897	0.244	0.074	0.005	15.011	3.165	0.989	6.181	168.285	3.281	-87.370
20	0.089	0.901	0.238	0.092	0.005	18.292	2.703	1.708	8.540	205.991	3.183	-88.550
21	0.007	7.955	0.161	2.000	3008.983	50.000	43.722	-46.000	-1150.000	7616.842	7.101	-57.250
22	0.006	6.791	0.137	0.033	0.003	10.833	164.239	-0.833	-8.330	1682.012	3.120	-89.330
23	0.006	6.191	0.116	0.050	0.004	12.443	113.252	3.557	22.231	1961.937	3.070	-89.960
24	0.006	6.417	0.103	0.059	0.004	13.208	91.255	6.792	33.960	2100.108	3.043	-90.300

Supplemental Table 6. Estimated kinetic parameters from simulations. Curve numbers related to curve simulated kinetic parameters in Supplemental Table 5. K_1 is relatively well estimated, however the BP_{ND} becomes unstable at low levels of K_1.

Time (min)	Activity (kBq/cc)
0.08	20.06
0.25	127.34
0.42	237.26
0.58	356.85
0.75	387.21
0.92	345.15
1.08	298.41
1.25	253.76
1.42	211.44
1.58	187.91
1.75	175.63
1.92	160.92
2.08	158.90
2.25	153.93
2.42	154.93
2.58	149.61
2.75	140.65
2.92	131.96
3.25	133.83
3.75	129.21
4.50	125.97
6.00	120.01
8.00	110.94
11.50	99.15
16.50	89.07
21.50	78.29
26.50	70.74
31.50	66.03
36.50	61.30
41.50	56.47
46.50	53.55
51.50	49.17
56.50	46.83
64.00	42.98
74.00	37.98

84.00	36.45
94.00	33.08
104.00	33.56
114.00	30.45

Supplemental Table 7. Input function data used for simulation work.

Time (min)	Parent fraction
2	0.95
5	0.82
10	0.81
20	0.81
30	0.77
60	0.54
120	0.69

Supplemental Table 8. Radiometabolite data used for simulation work.

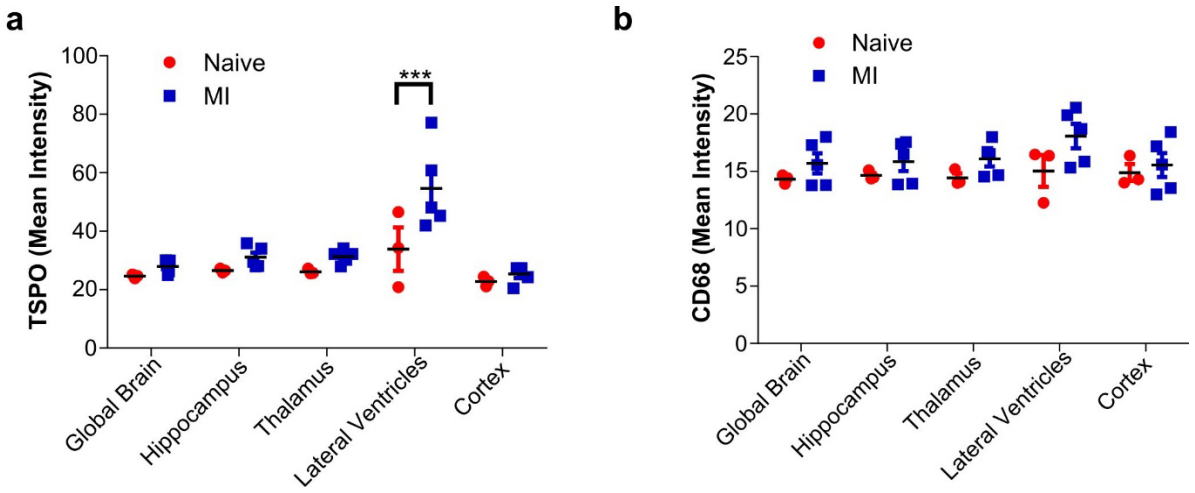

Supplemental Figure 15. Quantification of TSPO and CD68 immunofluorescent staining. A) TSPO signal within the brain and selected sub-regions of naive and MI rats. **B)** CD68 signal within the brain and selected sub-regions of naive and MI rats. Results represent the mean±S.E.M., naive *n* = 3, MI *n* = 5.

The Journal of NUCLEAR MEDICINE

Quantification of macrophage-driven inflammation during myocardial infarction with ^{18}F-LW223, a novel TSPO radiotracer with binding independent of the rs6971 human polymorphism

Mark G. MacAskill, Agne Stadulyte, Lewis Williams, Timaeus E. F. Morgan, Nikki L. Sloan, Carlos J. Alcaide-Corral, Tashfeen Walton, Catriona Wimberley, Chris-Anne McKenzie, Nick B. Spath, William Mungall, Ralph BouHaidar, Marc R. Dweck, Gillian A. Gray, David E. Newby, Christophe Lucatelli, Andrew Sutherland, Sally Pimlott and Adriana A. S. Tavares

J Nucl Med.
Published online: August 28, 2020.
Doi: 10.2967/jnumed.120.243600

The Journal of Nuclear Medicine is published monthly.
SNMMI | Society of Nuclear Medicine and Molecular Imaging
1850 Samuel Morse Drive, Reston, VA 20190.
(Print ISSN: 0161-5505, Online ISSN: 2159-662X)

SNMMI SOCIETY OF NUCLEAR MEDICINE AND MOLECULAR IMAGING